Journal of Analytical and Applied Pyrolysis 193 (2026) 107411

Contents lists available at ScienceDirect

Journal of Analytical and Applied Pyrolysis

journal homepage: www.elsevier.com/locate/jaap

Study on the performance and structure of low graphitized biochar prepared by silica template method for adsorbing odorous gases

Ruiying Wang [a], Fen Li [a,*], Hong Yan [a], Oxana P. Taran [b], Ying Yang [a], Dongdong Yang [a]

[a] Key Laboratory of Green Chemical Engineering and Technology of College of Heilongjiang Province, School of Materials Science and Chemical Engineering, Harbin University of Science and Technology, Harbin 150080, PR China
[b] Institute of Chemistry and Chemical Technology SB RAS, FRC "Krasnoyarsk Science Center SB RAS", Akademgorodok 50/24, Krasnoyarsk 660036, Russia

ARTICLE INFO

Keywords:
Hydrogen sulfide
Methyl mercaptan
Biomass
Graphitized carbon

ABSTRACT

Research on the removal of sulfur-containing malodorous gases from air via biochar adsorption demonstrates significant application potential. In this study, silicon-modified graphitized carbon was synthesized through pyrolysis using peanut shells, rice husks, and walnut shells as precursors. Among the resulting materials, rice husk-derived biochar (DK-700–5) and walnut shell-derived biochar (HT-800–10) exhibited pronounced targeted adsorption toward CH_3SH and H_2S, respectively. The sulfur adsorption capacity of DK-700–5 was 8.3 times higher than that of unmodified rice husk biochar, while HT-800–10 achieved a 2.45-fold enhancement in H_2S adsorption compared to its unmodified counterpart. Carboxyl and oxygen vacancies on DK-700–5 were identified as critical for CH_3SH adsorption, facilitating its immobilization and gradual oxidation to sulfate (SO_4^{2-}), with intermediate sulfur species such as R–SO–R, S°, and C–S detected. In parallel, HT-800–10 adsorbed and oxidized H_2S through its porous structure and surface superoxide radicals, converting it into elemental sulfur (S°) and sulfate (SO_4^{2-}), thereby achieving efficient adsorption and oxidative transformation.

1. Introduction

Sulfur-containing malodorous gases represent a major class of air pollutants that not only degrade environmental quality but also pose significant risks to human health [1]. Unlike conventional industrial gases such as CO_2, SO_2, or NO_x, these odorous gases typically exhibit extremely low odor thresholds (often at ppb levels), meaning that even trace concentrations can cause pronounced irritation, making their treatment more challenging than that of common gaseous pollutants. Among malodorous gases, hydrogen sulfide (H_2S) and methyl mercaptan (CH_3SH) are the most representative. Both are highly toxic, strongly odorous, and commonly released from sources such as sewage treatment, livestock farming, and biomass decomposition. H_2S, as an inorganic sulfur gas, displays high diffusivity, whereas CH_3SH, as an organic sulfur compound, shows strong affinity for reactive surface sites. Their co-existence, coupled with contrasting chemical properties, makes them ideal model compounds for investigating malodorous gas adsorption [2–6].

Adsorption has garnered increasing attention due to its operational simplicity, cost-effectiveness, and high deodorization efficiency [7]. In particular, biochar derived from biomass wastes—such as agricultural residues, forestry by-products, sludge, and animal manure—has emerged as a sustainable and low-cost adsorbent [8]. Converting these wastes into carbon-rich materials not only facilitates resource recycling but also contributes to atmospheric CO_2 mitigation. Numerous studies have demonstrated the environmental remediation potential of biochar, embodying the principle of "treating waste with waste." For instance, banana pseudostem biochar has been employed to purify hydrogen sulfide in biogas, achieving a sulfur adsorption capacity of 2.09 mg/g [9]. It is widely acknowledged that increased porosity and surface area enhance biochar's adsorption performance [10]. For example, KOH-activated corn straw biochar with a surface area of 2183.80 m^2/g exhibited superior adsorption of Cr(VI) and naphthalene, with theoretical monolayer adsorption capacities of 116.97 mg/g and 450.43 mg/g, respectively [11]. However, when the specific surface area reduced to 289 m^2/g, the adsorption capacity of naphthalene is only 106.75 mg/g [12].

However, most biochars reported for odorous gas adsorption, despite possessing large specific surface areas, are predominantly composed of amorphous carbon with a disordered layer structure. If the pore size

* Corresponding author.
E-mail addresses: 2596603713@qq.com (R. Wang), hgxylf@126.com (F. Li), yanhong204821@aliyun.com (H. Yan), taran.op@icct.ru (O.P. Taran), yangyinglake@126.com (Y. Yang), 1946858250@qq.com (D. Yang).

https://doi.org/10.1016/j.jaap.2025.107411
Received 17 July 2025; Received in revised form 9 September 2025; Accepted 29 September 2025
Available online 30 September 2025

distribution of such biochars does not align with the dimensions of the target odor molecules, mass transfer limitations may impede the rapid and efficient capture of odor gases. Previous studies have indicated that biochar with a graphitized structure can markedly enhance pollutant removal efficiency due to its well-ordered pore architecture. For instance, compared to raw biochar, the adsorption efficiency for organic pollutants in water increased by nearly 162-fold [13]. Moreover, other reports suggest that minor defects within graphite structures may further promote adsorption [14]. Despite these insights, the role of graphitized biochar in the adsorption of odorous gases remains poorly understood, representing a clear knowledge gap.

Additionally, the degree of graphitization is recognized as a crucial structural parameter that significantly influences the adsorption performance of carbon-based materials [15]. Compared with highly graphitized carbon, biochar with a low graphitization structure can generally be obtained at relatively low pyrolysis temperatures. Such biochar not only possesses a certain amount of ordered pores but also contains structural defects and abundant oxygen-containing functional groups, providing additional active adsorption sites and enhancing interactions with polar molecules. For odorous sulfur-containing gases such as CH_3SH and H_2S, these structural defects and surface functional groups facilitate stronger binding and catalytic adsorption pathways, thereby improving capture efficiency. Emphasizing low-graphitization carbon structures not only differentiates our material design from conventional highly graphitized adsorbents but also highlights the potential advantages of this hybrid disordered–ordered carbon framework in addressing odor gas adsorption challenges. To achieve more layered pore structures in biochar, silicon-template-assisted modification offers an effective strategy. Incorporating silica scaffolds during pyrolysis facilitates the formation of well-developed mesoporous and macroporous architectures within the carbon matrix. The stress distribution and local structural features of the pore walls can further promote the rearrangement of aromatic layers, thereby enhancing local graphitization, improving gas diffusion pathways, and preserving the active functional groups of biochar. Such a dual effect is anticipated to markedly strengthen the adsorption of volatile sulfur compounds. On this basis, the present work focuses on the development of silicon-templated, low-graphitization biochar and provides a systematic evaluation of its structural characteristics and adsorption behavior toward two representative malodorous gases, H_2S and CH_3SH. The results offer a practical guideline for the rational design of biochar-based materials for deodorization applications.

2. Materials and methods

2.1. Preparation of materials

The process flow of preparing biomass graphitized carbon by pyrolysis method is shown in Fig. 1.

Approximately 2 g of biomass powder was carbonized under a nitrogen atmosphere at different heating rates (5 °C/min, 10 °C/min, and 15 °C/min) and pyrolysis temperatures (400°C, 500°C, 600°C, 700°C, and 800°C) for 2 h. After cooling the pyrolyzed samples to 70°C, the resulting crude carbon products were collected and labeled according to their biomass source, pyrolysis temperature (X), and heating rate (Y): peanut shell-derived carbon as "HSB-X-Y," hickory nut shell-derived carbon as "HTB-X-Y," and rice husk-derived carbon as "DKB-X-Y."

For silicon-template-assisted modification, 2 g of biomass powder was thoroughly mixed with 2 g of Na_2SiO_3 and then pyrolyzed under a nitrogen atmosphere. The pyrolyzed product was subsequently immersed in 50 mL of NaOH solution for 48 h, followed by repeated washing with deionized water and filtration until the filtrate reached neutral pH. The resulting material was dried at 70°C to obtain graphitized biomass carbon. The prepared graphitized carbons derived from peanut shells, hickory nut shells, and rice husks were designated as "HS-X-Y," "HT-X-Y," and "DK-X-Y," respectively. Additionally, the corresponding adsorption-saturated graphitized carbons were labeled as "HSH-X-Y" (peanut shell-derived), "HTH-X-Y" (hickory nut shell-derived), and "DKH-X-Y" (rice husk-derived). Please refer to Table 1 for detailed material naming.

2.2. Adsorption performance test

The adsorption test setup is illustrated in Fig. 2. H_2S (99.97 ± 3 ppm) and CH_3SH (50.58 ± 3 ppm) were used as target odorous gases, with N_2 serving as the balance gas. The adsorbent material was loaded into a plexiglass reactor, and the system's connectivity and airtightness were verified. Gas was introduced from the cylinder, and the pressure regulator was adjusted to maintain a flow rate of 17 ± 1 mL/min, as monitored by a rotameter. Gas concentrations at the reactor outlet were measured every 3 min using a gas chromatograph (GC-9160, Shanghai Ouhua Analytical Instrument Factory). When the H_2S or CH_3SH concentration at the outlet exceeded 20.0 ppm, the pressure regulator was closed to stop gas inflow, and the time elapsed from adsorption initiation to termination was recorded as the material's odorous gas adsorption

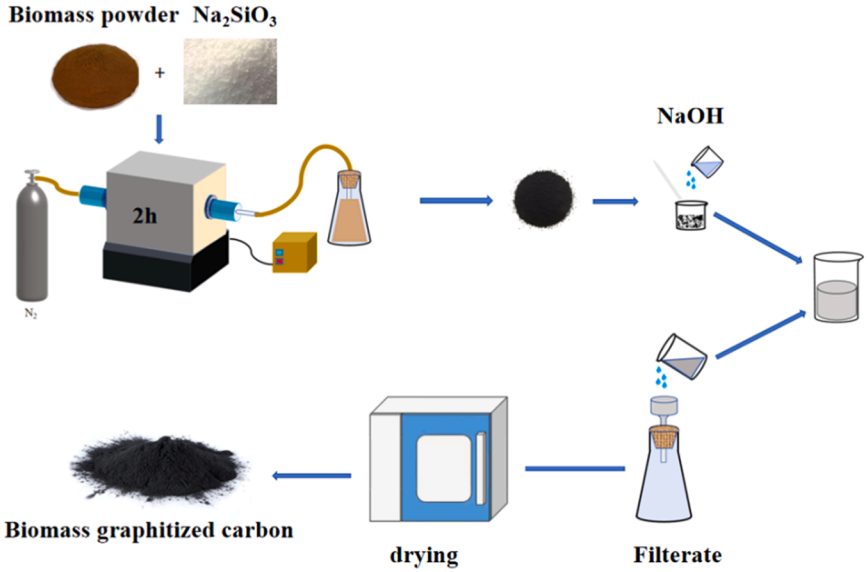

Fig. 1. Preparation process diagram of biomass graphitized carbon.

Table 1
Summary of sample naming rules.

Biomass Source	Pyrolysis Temperature (X)	Heating Rate (Y)	Carbonization Treatment	Sample Name
Peanut shell	400°C, 500°C, 600°C, 700°C, 800°C	5 °C/min, 10 °C/min, 15 °C/min	Direct pyrolysis	HSB-X-Y
Hickory nut shell	400°C, 500°C, 600°C, 700°C, 800°C	5 °C/min, 10 °C/min, 15 °C/min	Direct pyrolysis	HTB-X-Y
Rice husk	400°C, 500°C, 600°C, 700°C, 800°C	5 °C/min, 10 °C/min, 15 °C/min	Direct pyrolysis	DKB-X-Y
Peanut shell	400°C, 500°C, 600°C, 700°C, 800°C	5 °C/min, 10 °C/min, 15 °C/min	Template-assisted pore formation	HS-X-Y
Hickory nut shell	400°C, 500°C, 600°C, 700°C, 800°C	5 °C/min, 10 °C/min, 15 °C/min	Template-assisted pore formation	HT-X-Y
Rice husk	400°C, 500°C, 600°C, 700°C, 800°C	5 °C/min, 10 °C/min, 15 °C/min	Template-assisted pore formation	DK-X-Y
Peanut shell	400°C, 500°C, 600°C, 700°C, 800°C	5 °C/min, 10 °C/min, 15 °C/min	Adsorption Saturation	HSH-X-Y
Hickory nut shell	400°C, 500°C, 600°C, 700°C, 800°C	5 °C/min, 10 °C/min, 15 °C/min	Adsorption Saturation	HTH-X-Y
Rice husk	400°C, 500°C, 600°C, 700°C, 800°C	5 °C/min, 10 °C/min, 15 °C/min	Adsorption Saturation	DKH-X-Y

time.

For evaluation of mixed-gas adsorption performance (H_2S and CH_3SH), the total flow rate was maintained at 24 ± 1 mL/min, with gas flow ratios (CH_3SH:H_2S) tested sequentially at 1:2, 1:1, and 2:1.

Sulfur capacity, defined as the mass of H_2S or CH_3SH adsorbed per gram of material, was employed as the key metric for assessing the adsorption performance of graphitized biomass carbon. The sulfur capacity was calculated using the following equation [16]:

$$Q = \frac{qM}{wV_m}\left(C_0 t - \int_0^t C_t dt\right) \times 10^{-6} \quad (1)$$

where q denotes the inlet gas flow rate (mL/min), M is the molar mass (34 g/mol for H_2S and 48.1 g/mol for CH_3SH), C_o and C_t represent the inlet and outlet gas concentrations (ppm), respectively, t is the adsorption time (min), w is the mass of adsorbent (g), and V_m stands for the molar volume of gas at standard conditions (22.4 L/mol). This parameter served as a key indicator to quantitatively assess the adsorption performance of the graphitized biomass carbon for H_2S and CH_3SH removal.

2.3. Characterization of materials

The surface morphology of the carbon materials was examined using a ZEISS GeminiSEM 300 scanning electron microscope (Germany). Prior to imaging, the samples underwent vacuum filtration and were subsequently metallized via sputter coating. The microstructure of the graphitized biomass carbon was investigated using a JEOL JEM-2100F transmission electron microscope (Japan), with specimens prepared by ultrasonic dispersion in ethanol. Surface functional groups were characterized by Fourier-transform infrared spectroscopy (FT-IR, Thermo Scientific Nicolet iS20, USA), with samples mixed with KBr, ground, and pressed into pellets for analysis over the wavenumber range of 400–4000 cm^{-1} . Elemental composition of carbon, nitrogen, oxygen, silicon, and sulfur was analyzed using X-ray photoelectron spectroscopy (XPS, Thermo Scientific K-Alpha, USA) equipped with an Al-Kα X-ray source, employing 20–30 mg of sample material. Specific surface area and porosity were determined via Brunauer–Emmett–Teller (BET) analysis (Micromeritics ASAP 2460, USA) using nitrogen adsorption–desorption isotherms, with samples degassed at 200°C for 8 h prior to measurement. Additionally, the structural characteristics of the graphitized biomass carbon were probed by Raman spectroscopy (Horiba LabRAM HR Evolution, Japan) using a 532 nm laser excitation source, with spectral acquisition conducted over the 500–2000 cm^{-1} wavenumber range. Electron paramagnetic resonance spectroscopy was further employed to detect reactive oxygen species, including superoxide radicals ($\cdot O_2^-$) and the G values.

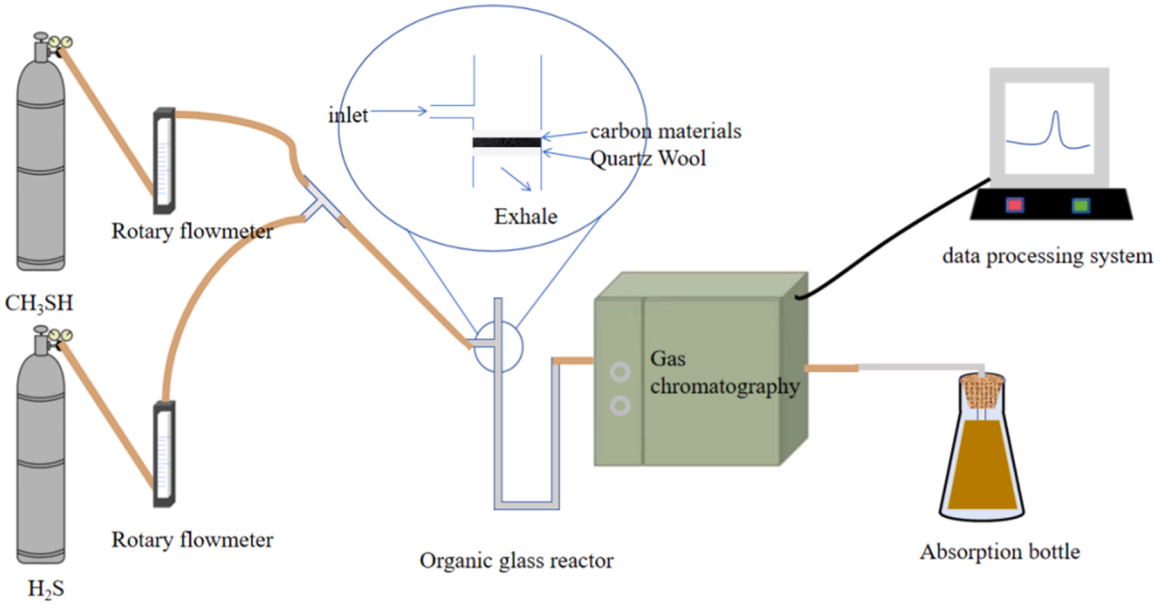

Fig. 2. Schematic diagram of adsorption testing device.

3. Results and discussion

3.1. Analysis of adsorption performance and graphitic structure of biochar

3.1.1. Analysis of graphitic structure

DK-700–5 and HT-800–10 were identified as the optimized materials exhibiting the highest targeted adsorption performance for hydrogen sulfide and methyl mercaptan, respectively (Fig. 7). The SEM and TEM images of DK-700–5 and HT-800–10 are presented in Figs. 3 and 4.

As shown in Fig. 3(a–c), rice husk-derived carbon, after pyrolysis and SiO_2 templating, formed a porous structure with distinct morphological features. Fig. 3(a) shows that the pyrolyzed carbon possesses a porous surface with small, densely distributed pores; the rough surface with irregular edges likely reflects the intrinsic morphology of the rice husk precursor, indicating preservation of the raw material characteristics. Fig. 3(b) displays the rice husk carbon prior to SiO_2 removal, where the pores appear larger and shallower compared to Fig. 3(a), with particulate SiO_2 observable on the pore walls. After SiO_2 removal, Fig. 3(c) shows more regularly arranged and significantly enlarged pores, confirming the critical role of SiO_2 in modulating the pore structure. TEM analysis of DK-700–5 (Fig. 4b) further reveals "striated" or "layered" structures along the carbon edges, indicative of graphitized regions. The curvature of these layers suggests a limited degree of graphitization, while the hazy regions indicate the coexistence of amorphous carbon, consistent with the material's partially graphitized nature.

Fig. 3(d–f) depict the surface morphology of the walnut shell-derived carbon materials. In Fig. 3(d), the material exhibits a rough surface with densely distributed, relatively small pores, reflecting the inherent structure of the walnut shell precursor. Fig. 3(e) shows more irregular pore morphologies, where some enlarged pores approach the micrometer scale but appear shallower, suggesting that in situ formation and deposition of SiO_2 from Na_2SiO_3 during pyrolysis partially blocked the original pore channels. After SiO_2 removal (Fig. 3f), the material develops well-defined, uniformly distributed micrometer-scale channels. Notably, the pore walls contain visible micropores, and the carbon particles form an interconnected porous network. This hierarchical structure, combining macropores (facilitating efficient molecular transport) with wall micropores (providing enhanced surface area), creates an optimal architecture for gas adsorption. The macroporous channels serve as effective diffusion pathways, while the microporous walls supply abundant adsorption sites, explaining the improved performance observed in mixed-gas adsorption tests.

TEM characterization of different regions of HT-800–10 is presented in Fig. 4(a). In region I, distinct lattice fringes with an interlayer spacing of approximately 0.34 nm are observed, indicating the formation of graphitic layered structures. The curved and irregular nature of these fringes, however, suggests a limited degree of graphitization and the coexistence of disordered carbon components. Analysis indicates that at 800°C, HT-800–10 is in an early stage of graphitization, exhibiting partially ordered layered arrangements without forming highly organized graphite structures. The slightly enlarged interlayer spacing relative to standard graphite may result from spatial constraints imposed by the SiO_2 template during carbon layer formation, which simultaneously introduces porosity and structural disorder.

Regions II and III reveal significant structural heterogeneity. The central area (II) displays relatively dense fringe patterns, suggesting locally enhanced graphitization, whereas the edge region (III) appears smoother, likely corresponding to porous structures or disordered carbon layers at the boundaries. This structural irregularity at the edges may be associated with SiO_2 particle removal during processing and could substantially influence the material's porosity and specific surface area.

In summary, both DK-700–5 and HT-800–10, which exhibited superior adsorption performance, feature a template-directed porous graphitic carbon architecture. This unique structure, combining partially graphitized domains with template-induced porosity, provides high surface area and optimized pore networks, accounting for their enhanced gas adsorption capabilities. The controlled disorder introduced by the templating process appears to create favorable structural features for odorous gas capture while maintaining sufficient graphitic order to ensure material stability (Fig. 5).

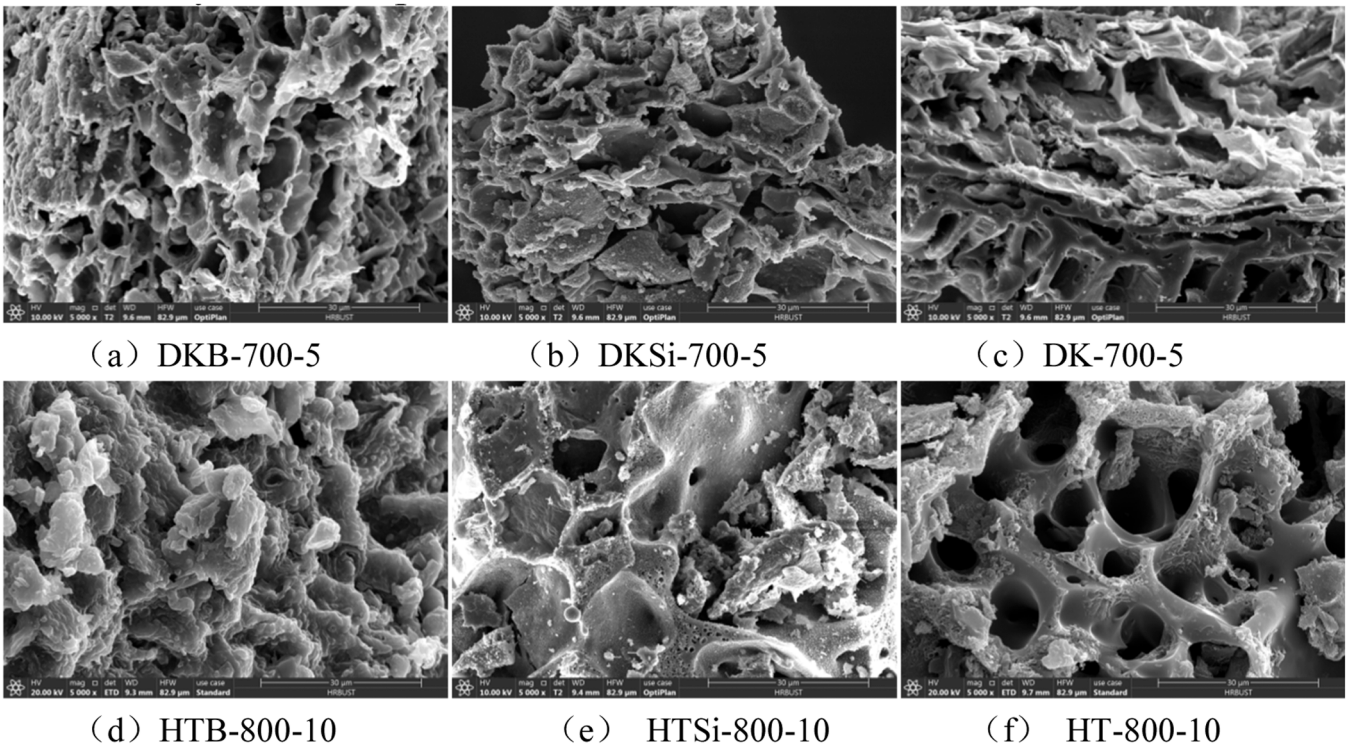

Fig. 3. SEM photos.

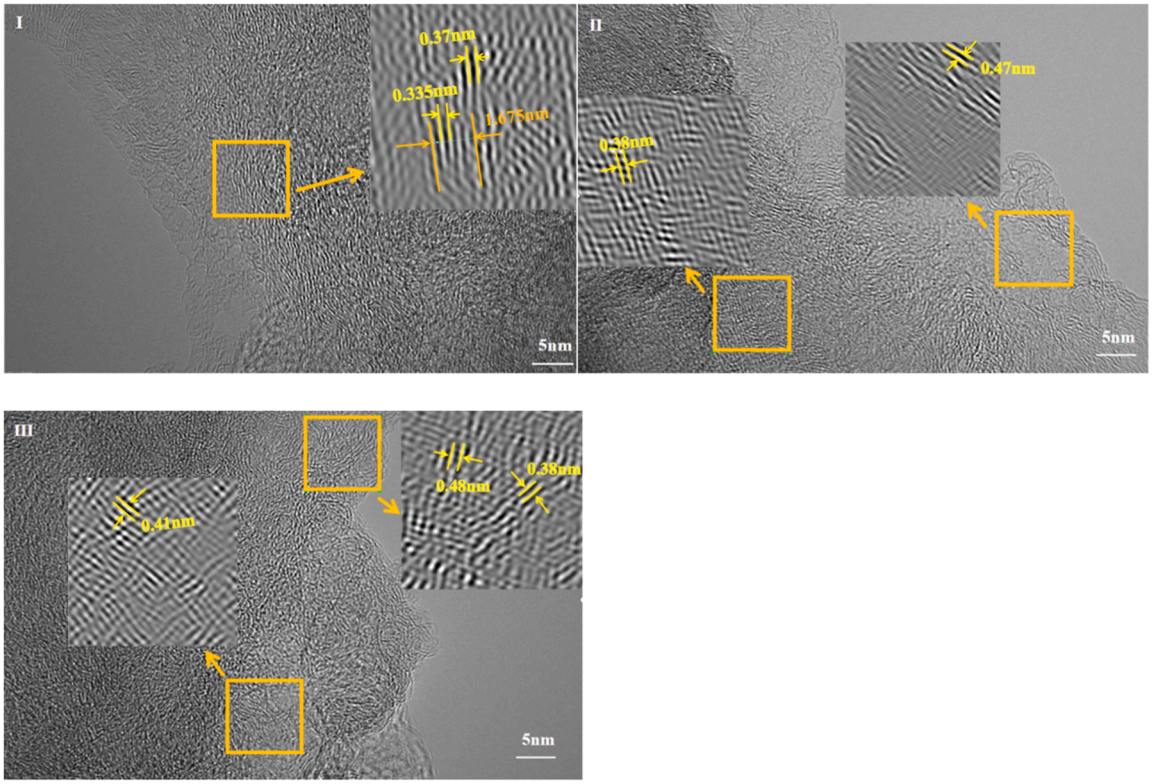

（a）HT-800-10

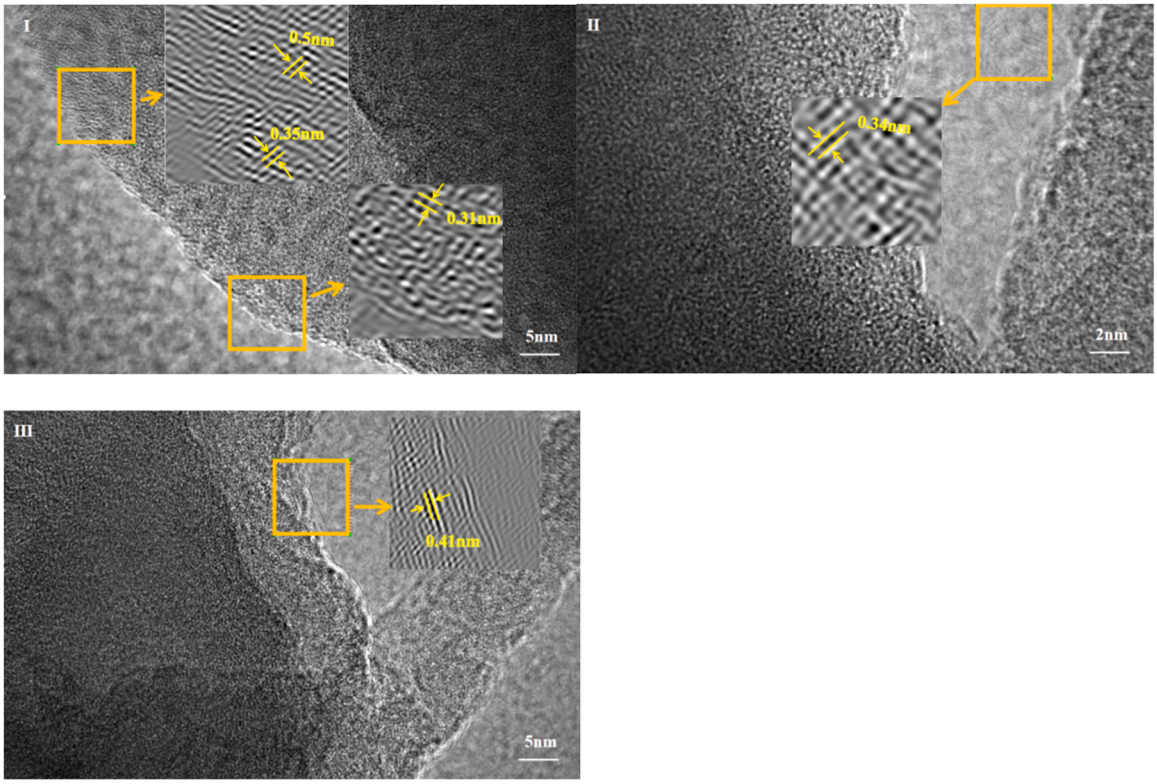

（b）DK-700-5

Fig. 4. TEM photos.

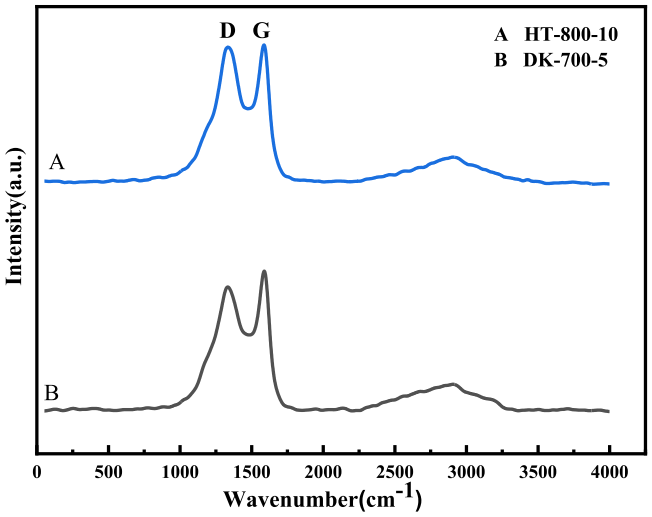

Fig. 5. Raman Spectrogram.

Raman spectroscopy was employed to investigate the structural ordering of the prepared biomass-derived graphitized carbon materials and their evolution during the adsorption process. All samples exhibited characteristic D bands (~1350 cm^{-1}) and G bands (~1580 cm^{-1}), corresponding to sp^3 -hybridized disordered carbon and sp^2-hybridized graphitic lattice structures, respectively. The D and G bands were deconvoluted using a two-peak Gaussian fitting method, and the intensity ratio (I_D/I_G) was calculated. The I_D/I_G values for DK-700–5 and HT-800–10 were determined to be 1.016 and 1.081, respectively, indicating that both materials are typical low-graphitization carbons [17]. Using the Tuinstra–Koenig relation (λ = 532 nm), the corresponding in-plane crystallite sizes (La) were estimated to be 4.33 nm and 4.07 nm, further confirming the underdeveloped nature of the graphitic domains [18].

The relatively high I_D/I_G ratios and small in-plane crystallite sizes (La) indicate that DK-700–5 and HT-800–10 possess a low degree of graphitization, abundant structural defects, and disordered carbon domains. These defects and edge sites generate numerous high-energy adsorption sites, which can effectively interact with polar odor molecules such as CH_3SH and H_2S via surface adsorption or chemical bonding [19]. Consequently, the low degree of graphitization endows the biochar with excellent adsorption performance for odorous gases [20].

3.1.2. *H_2S and CH_3SH single component odor adsorption performance*

The adsorption performance of biomass charcoal prepared from different raw materials at different pyrolysis temperatures and heating rates for CH_3SH and H_2S is shown in Fig. 6.

As shown in Fig. 6, the DKB series exhibited superior CH_3SH

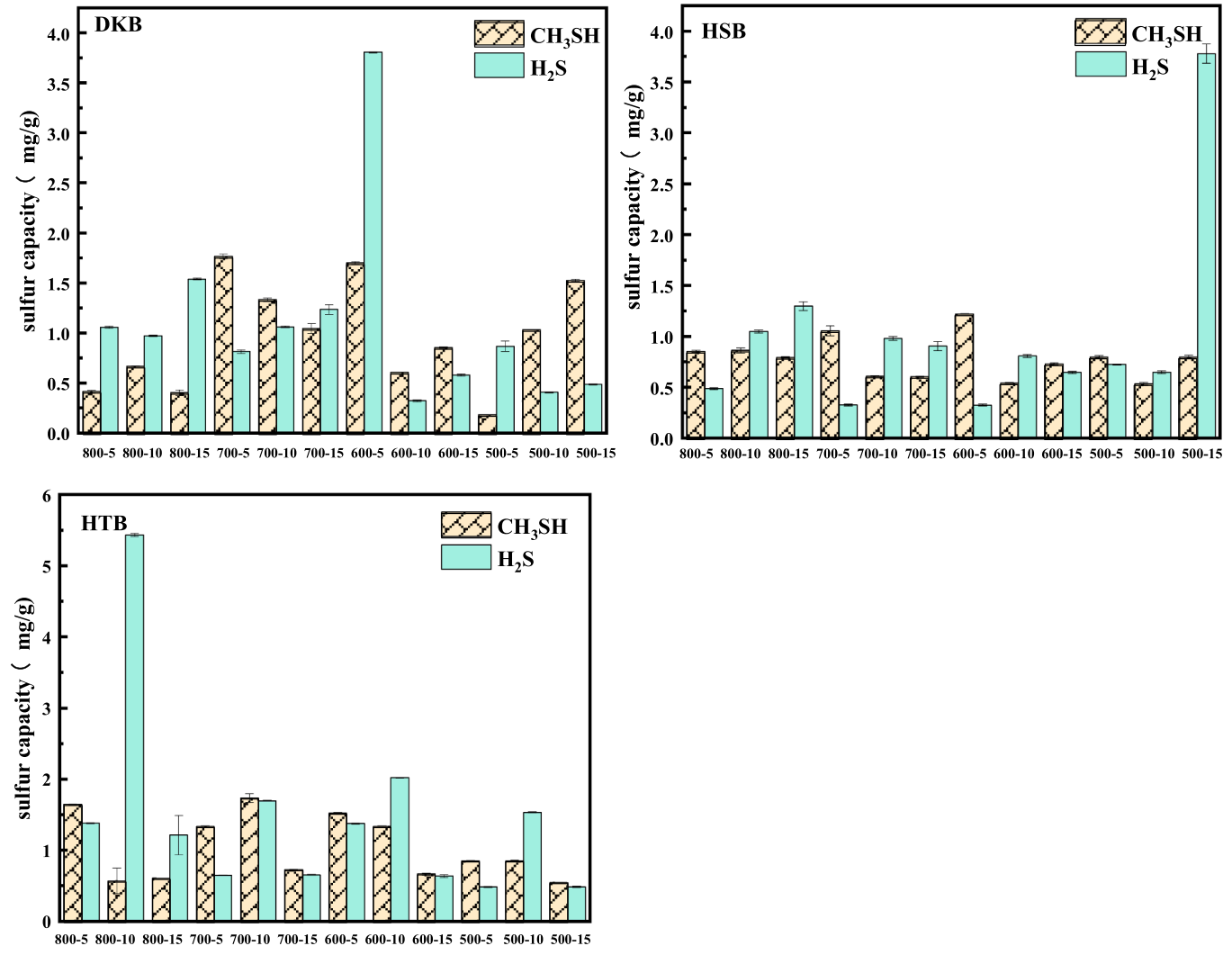

Fig. 6. Adsorption of H_2S and CH_3SH single component odor by crude char products.

adsorption performance, with sulfur capacities ranging from 0.5 to 2 mg/g, indicating strong adsorption capability toward CH_3SH. In contrast, the HSB samples showed relatively poor CH_3SH adsorption. The HTB series displayed intermediate performance, with sulfur capacities between 0.5 and 1.5 mg/g, positioning its adsorption capability between that of DKB and HSB.

For H_2S adsorption, the HTB series achieved sulfur capacities of approximately 1.5–5.5 mg/g, with HTB-800–10 reaching the highest value of 5.5 mg/g. Other samples under different conditions exhibited similar adsorption durations but lower capacities of around 1–2 mg/g, indicating weaker H_2S adsorption performance.

In summary, the optimal materials for CH_3SH and H_2S adsorption among the directly pyrolyzed carbonized samples were identified as DKB-700–5 and HTB-800–10, respectively. These results suggest that the biomass type, pyrolysis temperature, and heating rate significantly affect the adsorption performance of the resulting carbon materials.

To enhance the adsorption performance for CH_3SH and H_2S, the carbon materials with superior adsorption capacities were further modified. Prior to pyrolysis, Na_2SiO_3 was uniformly mixed with the raw biomass powder at a 1:1 mass ratio. The mixture was then pyrolyzed under the optimal temperature and heating rate conditions (700°C at 5 °C/min for CH_3SH-adsorbing DKB and 800°C at 10 °C/min for H_2S-adsorbing HTB). During pyrolysis, Na_2SiO_3 underwent in situ transformation to SiO_2 ($2Na_2SiO_3 + 2H_2O \rightarrow 2NaOH + SiO_2 + H_2 + 2H_2O$), which deposited on the biochar surface or within its pores.

The pyrolyzed carbon materials were subsequently immersed in NaOH solution to dissolve and remove the SiO_2 template via vacuum filtration, yielding modified porous carbon structures. Adsorption tests on these modified materials (Fig. 7) showed markedly enhanced performance compared to their unmodified counterparts.

As shown in Fig. 7(a), the modified HT-700–10 and DK-700–5 exhibited markedly enhanced methyl mercaptan (CH_3SH) adsorption capacities. Notably, DK-700–5 demonstrated an approximately 8.3-fold improvement, achieving a remarkable CH_3SH sulfur capacity of 15.8 mg/g. In comparison, modified DK-600–5, HT-600–5, and HT-500–5 showed only modest increases in CH_3SH adsorption.

Fig. 7(b) illustrates that the modified HT-800–10, DK-700–10, and DK-600–5 exhibited substantial enhancements in hydrogen sulfide (H_2S) adsorption performance. Among these, DK-600–5 achieved an exceptional H_2S sulfur capacity of 18 mg/g. These results clearly indicate that SiO_2 templating modification significantly improves the adsorption performance of the carbon materials for both H_2S and CH_3SH. The observed enhancements are likely attributable to the increased specific surface area and optimized pore structures introduced by the SiO_2 template, which expose more active adsorption sites and facilitate greater uptake of gas molecules. This templating strategy effectively tailors both the porosity and surface chemistry of the biomass-derived carbons, resulting in superior adsorption capabilities for sulfur-containing odorous gases.

3.1.3. Adsorption performance of H_2S and CH_3SH mixed odor

Fig. 8 presents the sulfur capacities of various graphitized biomass carbons for CH_3SH and H_2S adsorption under different gas flow ratios (CH_3SH:H_2S = 1:2, 1:1, 2:1). Under mixed-gas conditions, significant differences in adsorption performance were observed among the samples, with HT-800–10, HT-700–10, and DK-700–5 exhibiting markedly superior adsorption for both odorous components compared to DK-700–10 and DK-600–5. At a 1:1 flow ratio, HT-800–10 achieved optimal H_2S adsorption, reaching a remarkable sulfur capacity of 20 mg/g.

For DK-700–5, the adsorption performance toward the CH_3SH and H_2S mixture initially increased and then decreased as the flow ratio changed from 1:2–2:1. At the 1:1 flow ratio, DK-700–5 displayed the highest adsorption capacity for CH_3SH, with a sulfur capacity of 16 mg/g, while its H_2S adsorption was lower than that of HT-800–10. In summary, at a gas flow ratio of 1:1, DK-700–5 exhibits targeted adsorption of CH_3SH, whereas HT-800–10 demonstrates a more advantageous adsorption for H_2S.

3.2. Analysis of deodorization structure

3.2.1. FT-IR analysis

Fig. 9 (A) shows the distinct FT-IR spectral features of HT-800–10. A broad and intense absorption band at 3500–3200 cm^{-1} indicates the presence of hydroxyl (O–H) groups and potentially amine (N–H) functionalities in the graphitized carbon. These hydroxyl groups likely originate from surface-adsorbed water molecules or oxygen-containing functional groups (e.g., alcoholic hydroxyls) formed during pyrolysis. The weak absorption band at 1700–1600 cm^{-1} corresponds to C═O stretching vibrations, which may be attributed to carboxyl groups. Notably, the pronounced C–O stretching vibrations observed at

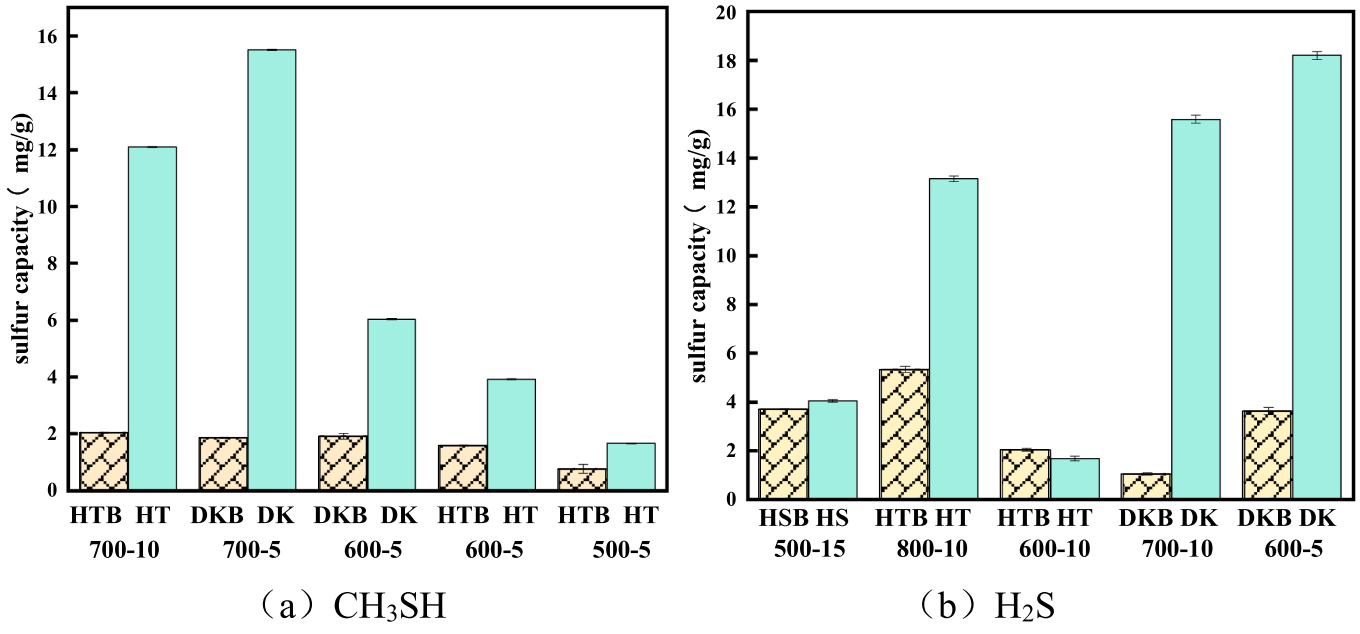

Fig. 7. Comparison of Sulfur Capacity of Biomass Charcoal for Adsorption of H_2S and CH_3SH Single Component Odor before and after Modification.

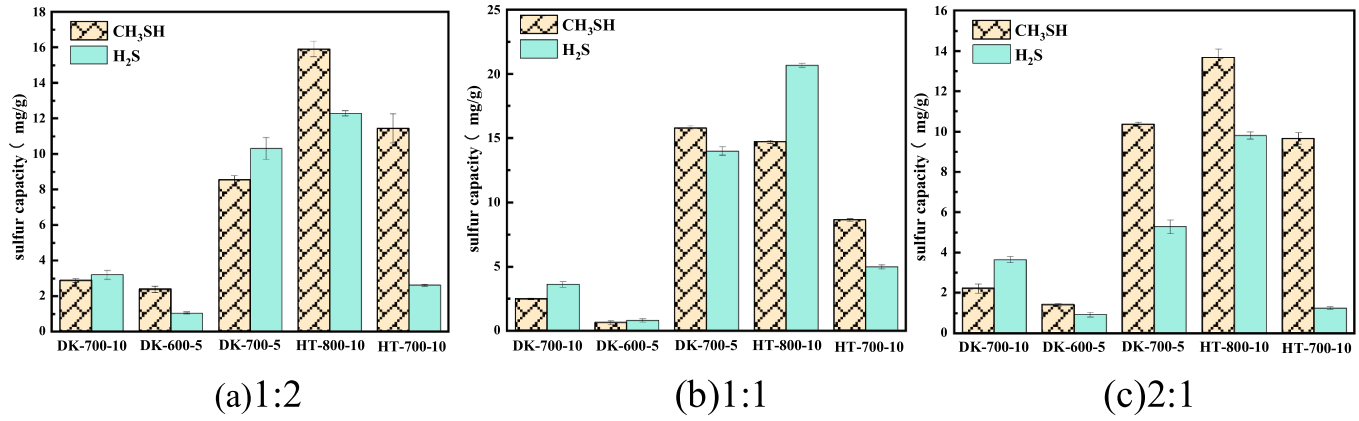

Fig. 8. Performance of Biochar in Adsorption of H_2S and CH_3SH Mixed Odor.

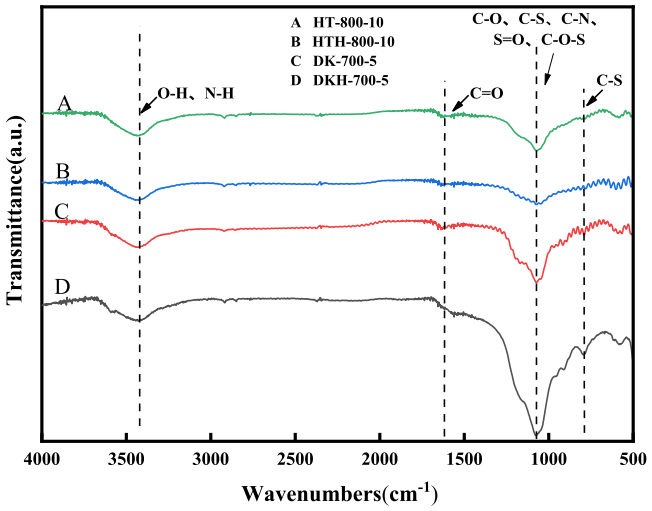

Fig. 9. FT-IR spectrum.

1200–1000 cm^{-1} suggest the presence of alcoholic hydroxyl compounds [21,22]. The abundant O–H and C–O functionalities in HT-800–10 are characteristic of high-temperature pyrolyzed biomass-derived graphitic carbon, likely resulting from cellulose/hemicellulose dehydration or recombination of pyrolysis intermediates. Comparative analysis of H_2S-saturated HTH-800–10 (Fig. 9B) shows significant attenuation of absorption bands at 3500–3200 cm^{-1} and 1200–1000 cm^{-1} , along with disappearance of the C═O signal at 1700–1600 cm^{-1} . These changes indicate that H_2S primarily interacts with hydroxyl and carboxyl groups via hydrogen bonding and acid–base interactions, with these oxygen-containing groups serving as the main active sites for H_2S adsorption [23]. These results demonstrate that oxygen functional groups, particularly C–O moieties, play a crucial role in H_2S capture, providing atomic-level insights into the adsorption mechanism of the developed carbon materials.

FT-IR analysis of the DKH-700–5(Fig. 9D) sample revealed that CH_3SH adsorption significantly altered the surface chemical properties of the material. Compared to DK-700–5(Fig. 9 C), the CH_3SH-saturated DKH-700–5 exhibited a slightly attenuated absorption band at 3500–3200 cm^{-1} , while the weak C═O band at 1700–1600 cm^{-1} nearly disappeared. In contrast, the S═O absorption peak at 1050 cm^{-1} increased markedly, which may result from CH_3SH adsorption on DKH-700–5 via van der Waals interactions or hydrogen bonding. Alternatively, CH_3SH could be oxidized to SO_4^{2-}, with intermediate products such as R–SO–R (sulfoxides) forming during the oxidation process [24]. Additionally, the signals at 1050 cm^{-1} (S-CO) and 850 cm^{-1} (C–S) likely arise from reactions between CH_3SH and carboxyl groups on the DK-700–5 surface, leading to thioester formation [25,26]. The disappearance of the C═O band combined with the enhancement of C–S signals suggests that CH_3SH chemically reacted with active sites on the biochar surface through its sulfur atoms.

3.2.2. XPS

Fig. 10 shows that the dominant C–C peak indicates the presence of a substantial amount of graphitized carbon in DK-700–5. The binding energy at 289.6 eV corresponds to O–C═O, suggesting that the sample contains highly oxidized biomass-derived graphitic carbon. These oxygen-containing functional groups facilitate the adsorption of methyl mercaptan (CH_3SH). The N 1 s spectrum reveals multiple chemical states of nitrogen in the sample. The N 1 s peak at 400.3 eV is assigned to pyrrolic nitrogen [27]. The lone pair electrons of pyrrolic-N can act as hydrogen-bond acceptors, interacting with the –SH group of CH_3SH. In addition, under conditions where CH_3SH partially dissociates and releases protons, pyrrolic-N may be protonated to form $–NH^+$, which further enhances the affinity and immobilization of sulfur species on the biochar surface. The O 1 s spectrum further elucidates the chemical states of oxygen, with binding energy peaks at 532.8 eV and 530.8 eV corresponding to C–O in carboxyl groups (O–C═O). The peak at 530.8 eV also indicates the presence of chemisorbed oxygen species (O^-), which exhibit oxidative properties and can directly oxidize CH_3SH [28] to SO_2, with further oxidation potentially leading to SO_4^{2-} formation ($SO_2 + O^- \rightarrow SO_3 \rightarrow SO_4^{2-}$).

Fig. 11 presents the XPS spectra of DKH-700–5 following CH_3SH adsorption. In the C 1 s spectrum, the dominant peak shifts to C–S, while the fitted peak positions of N 1 s and O 1 s remain largely unchanged compared to DK-700–5. However, the relative peak area percentages change before and after adsorption, as summarized in Table 2. Notably, the C–S peak area increases after CH_3SH adsorption consistent with the FT-IR observations. This suggests that CH_3SH molecules react with surface carboxyl groups, forming new functional groups such as C–S or S═O. The marked reduction in the proportions of C–O and O^- further confirms that oxygen-containing functional groups act as the primary reactive sites. The enhancement of the O–C═O peak after sulfide adsorption can be ascribed to two main factors. On the one hand, reactive oxygen species generated during the oxidation process may oxidize the carbon framework, leading to the formation of new carboxyl groups [29]. On the other hand, sulfur oxidation products (SO_4^{2-}) exhibit binding energies overlapping with the O–C═O region, which also contributes to the increased peak intensity. After CH_3SH adsorption, the peak shifted slightly to 400.0 eV, suggesting an increase in electron density due to hydrogen bonding or charge-transfer interactions between pyrrolic-N and CH_3SH. Meanwhile, the high-binding-energy component shifted from 406.3 to 405.2 eV, implying chemical environment changes or partial reduction of oxidized nitrogen species

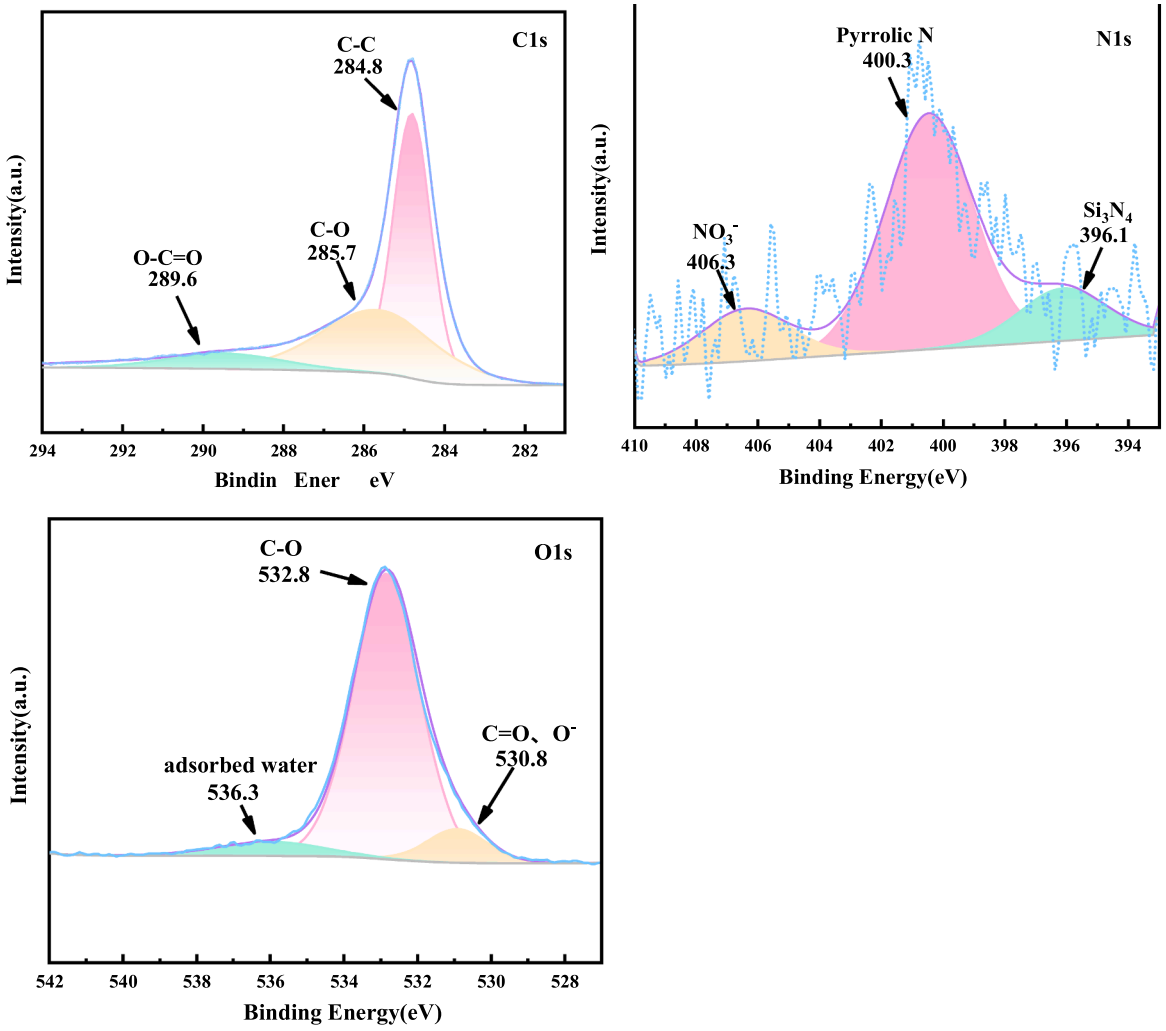

Fig. 10. XPS spectrum of DK-700–5.

(Table 3).

In summary, the abundant oxygen-containing functional groups (O–C═O) and chemisorbed oxygen species (O^-) in DK-700–5 provide active sites for CH_3SH adsorption. During the adsorption process, methyl mercaptan undergoes a series of chemical reactions on the carbon surface, forming sulfur-containing compounds and thereby achieving effective detoxification of CH_3SH.

Fig. 12 presents the XPS spectra of HT-800–10. The dominant C 1 s peak appears at 284.8 eV, indicating that graphitic carbon is the primary component. Two weaker peaks are observed at binding energies of 286 eV and 290 eV, corresponding to C–O and carboxyl groups (O–C═O), respectively [30]. The abundant surface oxygen-containing groups likely enhance the material's polarity, thereby facilitating the adsorption of polar molecules such as H_2S. The N 1 s spectrum is dominated by a peak at around 400.0 eV, assigned to pyrrolic nitrogen. This feature suggests that the biochar surface hosts nitrogen sites bearing lone-pair electrons, which may serve as potential active centers for interactions with sulfide species. The O 1 s spectrum shows a dominant peak at 532.2 eV, which can be mainly attributed to C-O species (alcohol groups) and the C-O component of carboxyl groups, along with a minor contribution from carboxyl C═O functionalities [31].

Fig. 13 presents the XPS spectra of HTH-800–10 after H_2S adsorption. After H_2S adsorption, the surface carbon functionalities of pecan shell biochar undergo significant changes. The relative proportion of C–C/C═C increases from 36.12 % to 51.92 %, whereas the C–O/C═O and O–C═O components decrease to 16.84 % and 3.82 %, respectively, indicating that hydroxyl, ether, carbonyl, and carboxyl groups participate in hydrogen bonding or acid–base interactions during adsorption. Meanwhile, SO_4^{2-}/S═O/S⁰ species appear at 20.71 %, reflecting partial oxidation of H_2S to elemental sulfur and sulfate on the biochar surface. These results suggest that H_2S adsorption involves not only physical adsorption and weak interactions, but also surface oxidation processes.

After H_2S adsorption, the N 1 s spectrum exhibits three components at 403.6, 400.2, and 397.7 eV. The 400.2 eV component corresponds to pyrrolic nitrogen, while the low-binding-energy peak at 397.7 eV likely represents electron-rich nitrogen sites, such as pyridinic-N or defect-associated nitrogen. These shifts indicate a rearrangement of the electronic environment of nitrogen during H_2S adsorption, reflecting changes in the chemical states and reactivity of surface [32].

3.2.3. *Analysis of specific surface area and pore structure*

As shown in Table 4, DK-700–5 possesses a specific surface area of 297.05 m^2/g, placing it within the medium-to-high range. This indicates that pyrolysis of rice husks generated a considerable number of effective adsorption sites, facilitating the capture of small molecules. Although not an ultra-high surface area material, DK-700–5 provides sufficient active sites for CH_3SH adsorption. The relatively small pore volume (0.17 cm^3/g) suggests that mesopores dominate the porosity, while the average pore diameter of 3.46 nm further confirms a primarily

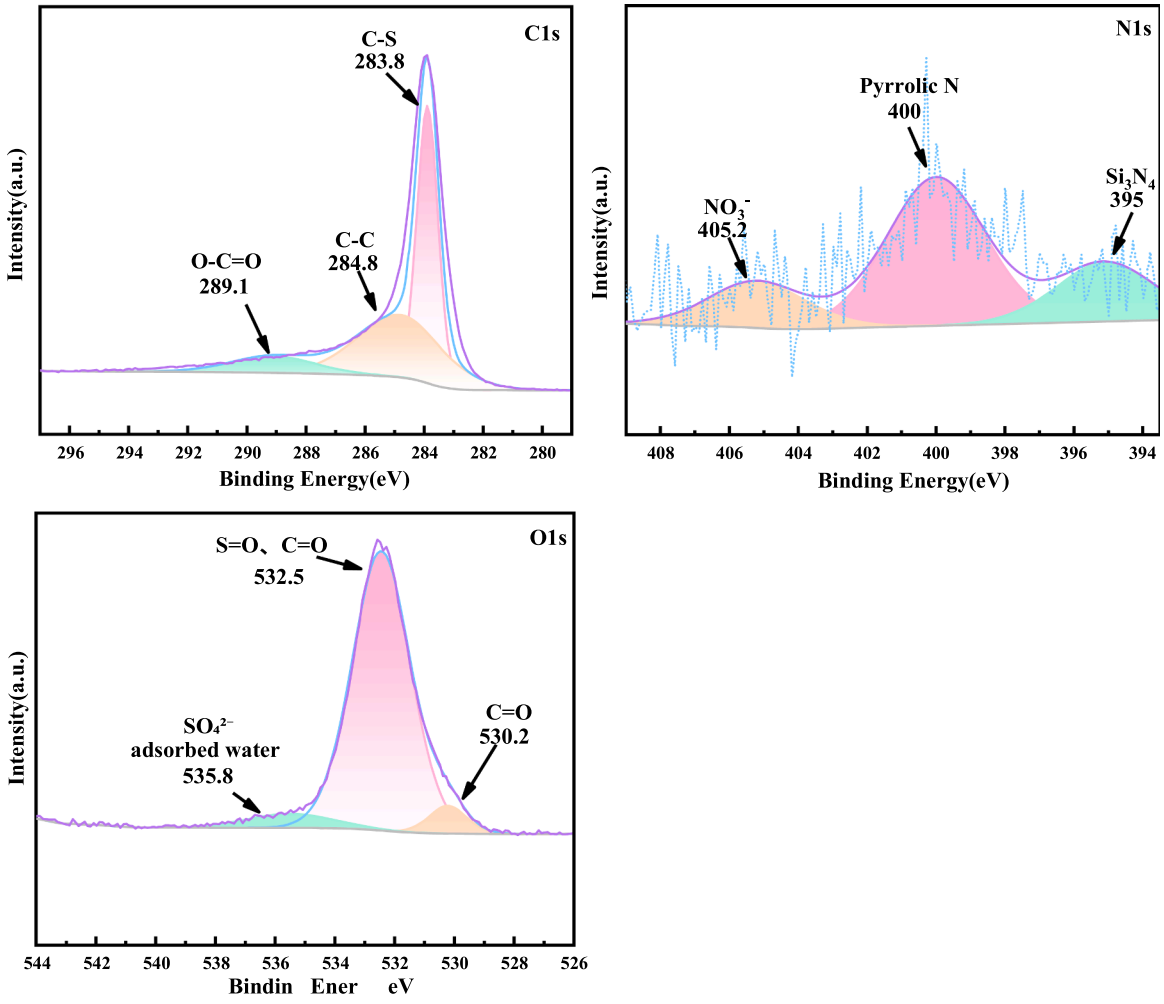

Fig. 11. XPS spectrum of DKH-700–5.

Table 2
Fitting data of DK-700–5.

Functional group	Relative area/%	
	DK-700–5	DKH-700–5
C-C	37.21	26.77
C-O	43.39	0
O-C═O	3.21	7.15
C-S	0	40.22
Pyrrolic N	0.85	0.86
O-、C═O	1.85	0
S═O、C═O	0	17.23
SO_4^{2-}、R-SO-R、S^0	0	1.65

Table 3
Fitting data of HT-800–10.

Functional group	Relative area/%	
	HT-800–10	HTH-800–10
C-C	36.12	51.92
C-O、C═O	48.46	16.84
O-C═O	7.77	3.82
pyrrolic nitrogen	1.38	0.95
SO_4^{2-}、S═O、S^0	0	20.71

mesoporous structure, offering favorable pathways for gas diffusion and adsorption. The low micropore proportion aligns with the limited adsorption capacity observed in the low-pressure region ($P/P_o < 0.1$) of the adsorption isotherm (Fig. 14a). Macropores mainly serve as transport channels, and their presence facilitates rapid access of CH_3SH molecules to mesopores and micropores, reducing mass transfer resistance during adsorption.

After CH_3SH saturation, the specific surface area of DKH-700–5 decreased to 134.95 m^2/g. This reduction can be attributed to pore occupation by adsorbed methyl mercaptan molecules, potential chemical reactions between CH_3SH and the graphitized carbon surface forming new functional groups, or pore-blocking effects. The pore volume decreased from 0.17 cm^3/g to 0.11 cm^3/g (~35 % reduction), indicating substantial pore occupation by CH_3SH or its derivatives. The more pronounced reduction in surface area (~54 %) suggests that adsorption predominantly occurred in high-surface-area micropores, corroborated by the noticeable decrease in micropore contribution.

HT-800–10 exhibits a relatively high specific surface area of 513.27 m^2/g and a pore volume of 0.1 cm^3/g, with a micropore proportion of 9.05 %. Compared to DK-700–5, the increased surface area primarily arises from micropores, despite the smaller pore volume. Mesopores account for nearly 50 % of the total porosity, providing abundant accessible surfaces for H_2S adsorption and facilitating gas diffusion and mass transfer, thereby enhancing adsorption efficiency. The moderate proportion of macropores further promotes transport into the internal pore network. After H_2S saturation, the specific surface area

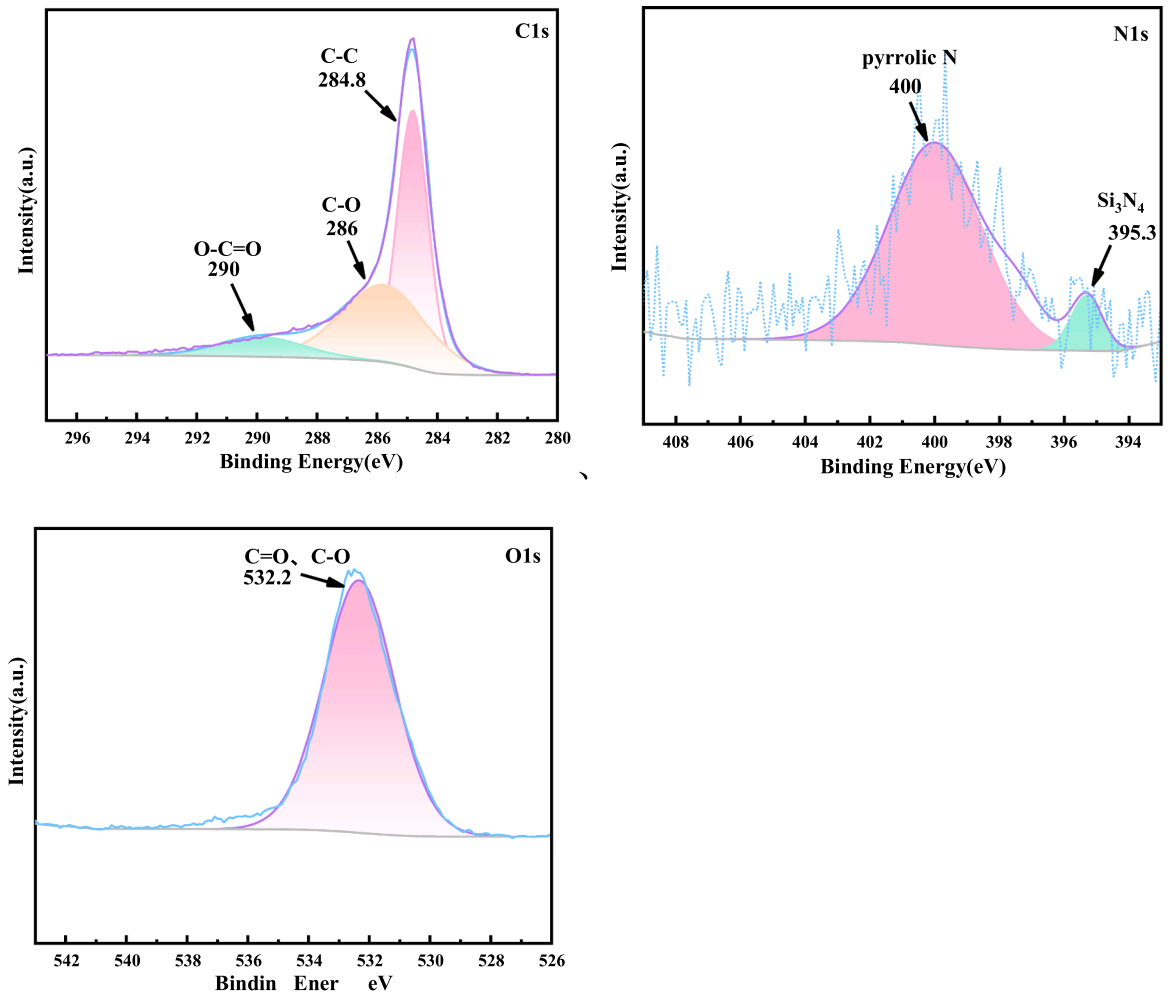

Fig. 12. XPS spectrum of HT-800–10.

decreased to 317.76 m^2/g, and the pore volume declined to 0.05 cm^3 /g, accompanied by a reduction in micropore contribution, indicating partial pore blockage by adsorbed H_2S molecules.

The relatively low micropore proportions in both DK-700–5 and HT-800–10 are primarily due to in-situ formation of silica templates from sodium silicate during pyrolysis. The resulting silica crystals occupy surface sites on the biomass-derived graphitic carbon. Upon subsequent silica removal, the previously occupied pore spaces remain, causing the collapse and widening of micropore walls into mesopores and inducing distortions in the graphitic layers. Considering the adsorption performance for CH_3SH and H_2S, it is concluded that a large specific surface area combined with a balanced distribution of mesopores and micropores is favorable. Mesopores facilitate molecular diffusion and accessibility, while remaining micropores provide high-energy adsorption sites, collectively enhancing gas capture efficiency.

From Fig. 14, the adsorption and desorption isotherms of DK-700–5 (Fig. 14a) exhibit a clear hysteresis loop characteristic of a Type IV isotherm, confirming the presence of a substantial mesoporous structure, which is favorable for CH_3SH adsorption. At low relative pressures ($P/P_o < 0.1$), the slow increase in adsorption capacity reflects the limited number of micropores. The hysteresis loop indicates possible capillary condensation within mesopores, contributing to enhanced adsorption. In the intermediate pressure range ($0.4 < P/P_o < 0.8$), the rapid increase in adsorption capacity demonstrates that mesopores are the dominant adsorption sites. At high relative pressures approaching $P/P_o = 1$, the continued increase in adsorption capacity, together with the macropore proportion of 22.79 %, indicates that macropores act as transport channels facilitating gas uptake. After CH_3SH adsorption, the isotherms in Fig. 14(c) show reduced adsorption capacity, consistent with the observed decreases in pore volume and specific surface area. The widening gap between the adsorption and desorption branches at $P/P_o > 0.5$ suggests altered adsorption behavior in mesopores and macropores, likely due to partial pore occupation or structural modifications.

Similarly, Fig. 14(b) shows that HT-800–10 exhibits Type IV adsorption-desorption isotherms, indicative of a predominantly mesoporous structure. At low relative pressures ($P/P_o < 0.1$), the rapid increase in adsorption capacity indicates the presence of micropores, consistent with the 9.05 % micropore contribution reported in Table 4. In the intermediate pressure range ($0.2 < P/P_o < 0.8$), the linear increase corresponds to capillary condensation in mesopores, highlighting their dominant role. At high relative pressures ($P/P_o > 0.8$), the further increase in adsorption capacity is attributed to macropores (17.81 %) and overall gas-filling effects. The distinct hysteresis loop reflects complex mesopore distributions, such as ink-bottle or irregular pore geometries, which enhance gas retention and adsorption stability. Fig. 14(d) indicates a similar trend post-adsorption, but with reduced adsorption capacity (from 100 to 200 cm^3/g to 50–100 cm^3/g), suggesting partial pore occupation or blockage. Importantly, the basic pore structure remains unchanged, indicating that H_2S adsorption reduces available pore volume and surface area without altering the fundamental meso- and macroporous architecture.

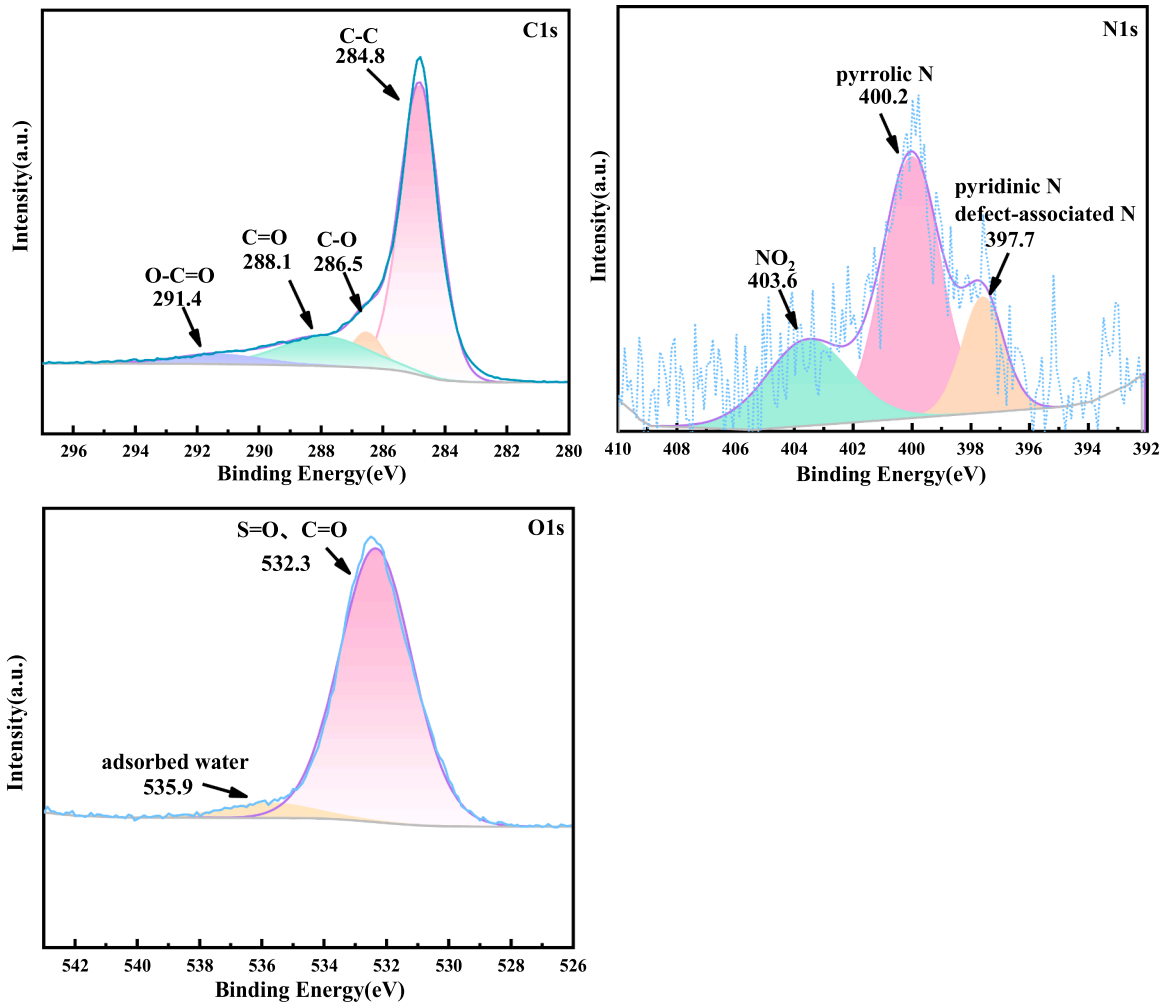

Fig. 13. XPS spectrum of HTH-800–10.

Table 4
Analysis of specific surface area and pore structure of biomass graphitized carbon.

Biomass graphitized carbon	specific surface area m^2/g	pore volume cm^3/g	Aperture nm	Pore size distribution %			
				≤ 2 nm	2–9.6 nm	9.6–43 nm	≥ 43 nm
DK−700–5	297.05	0.17	3.46	3.63	38.49	35.09	22.79
DKH−700–5	134.95	0.11	4.45	1.56	35.52	41.6	21.32
HT−800–10	513.27	0.1	2.14	9.05	48.12	25.02	17.81
HTH−800–10	317.76	0.05	2.11	5.74	41.12	26.56	26.58

3.3. adsorption mechanism

3.3.1. EPR

Fig. 15 presents the electron paramagnetic resonance (EPR) spectra of DK-700–5 and HT-800–10 under different magnetic field ranges. As shown in Figs. 15(a), DK–700–5 exhibits a g-value of approximately 2.003, which is commonly attributed to unpaired electrons associated with oxygen vacancies [33]. These oxygen vacancies serve as active sites that facilitate the adsorption of O_2 and its subsequent conversion into reactive oxygen species, such as superoxide radicals ($\cdot O_2^-$) and hydroxyl radicals ($\cdot OH$). Such radicals can directly oxidize CH_3SH, while the electron-rich environment near oxygen vacancies weakens the S–H bond, promoting dissociative adsorption ($CH_3SH \rightarrow CH_3S^- + H^+$) and enabling catalytic oxidation to CO_2 and SO_4^{2-} at room temperature in humid air [34]. Fig. 15(b) confirms the presence of superoxide radicals in HT-800–10, supporting their role in H_2S oxidation. In contrast, Fig. 15(c) shows that the hydroxyl radical signals for both DK-700–5 and HT-800–10 are relatively weak, suggesting that $\cdot OH$ plays a minor role in the adsorption and oxidation processes of CH_3SH and H_2S.

Overall, the EPR analysis indicates that the presence of oxygen vacancies in DK-700–5 and superoxide radicals in HT-800–10 contributes to their enhanced adsorption and catalytic oxidation of CH_3SH and H_2S, respectively, highlighting the critical role of defect engineering in the design of high-performance biochar-based adsorbents.

3.3.2. XPS

Fig. 16(a) shows that the S 2p spectrum of DKH-700–5 contains signals corresponding to SO_4^{2-}, R-SO-R, S^0, and C-S, indicating the multiple pathways involved in CH_3SH adsorption. DK-700–5 possesses a porous structure with abundant surface functional groups (C═O, C-O, etc.), enabling both physical and chemical adsorption of methanethiol. Its high specific surface area and hierarchical pore structure facilitate

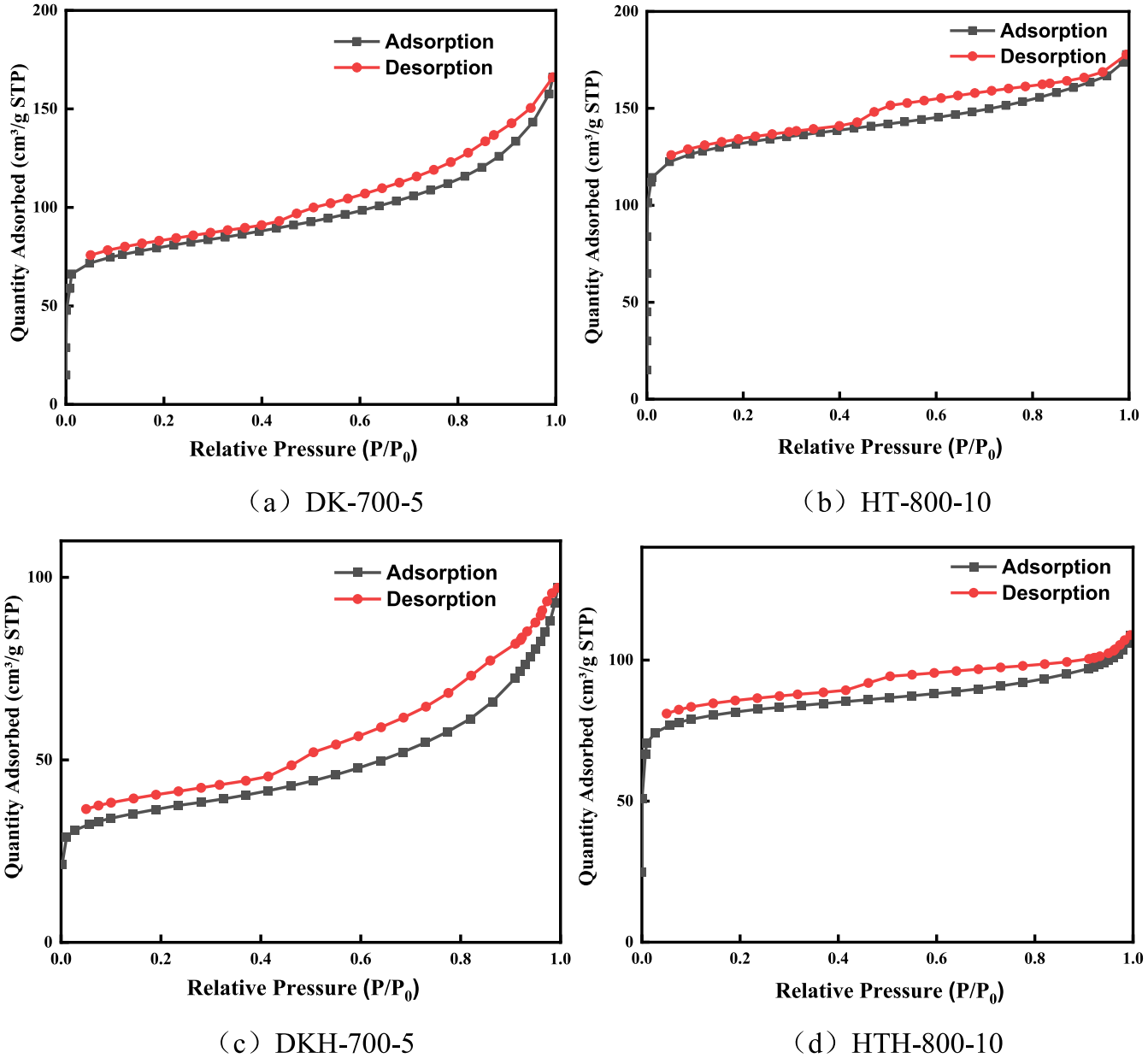

Fig. 14. Isothermal adsorption desorption curve.

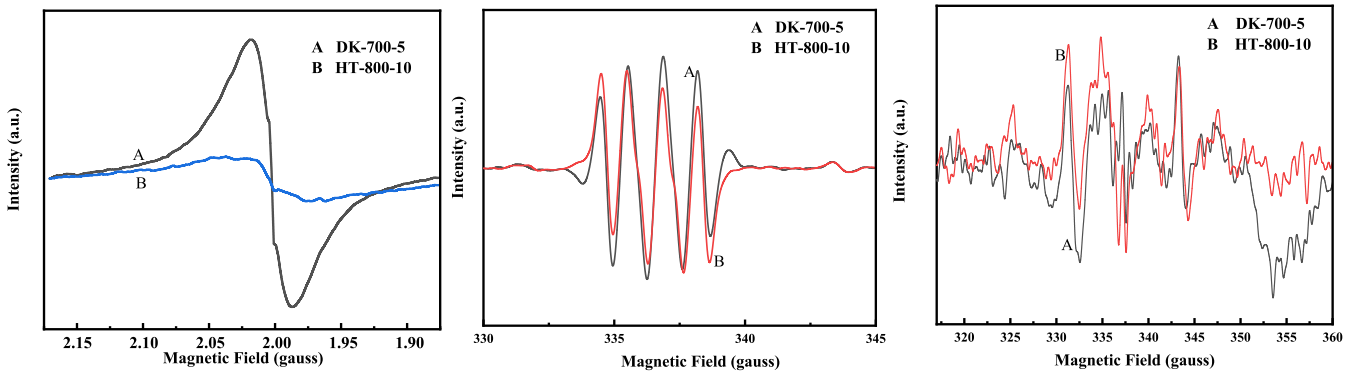

Fig. 15. EPR analysis.

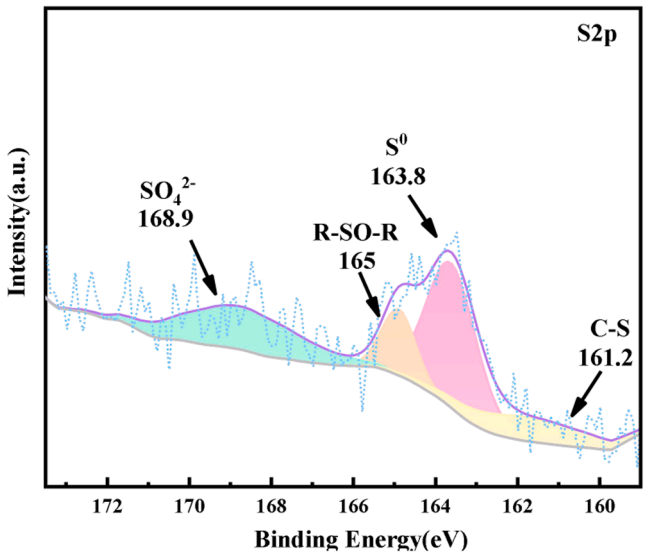

（a）DKH-700-5

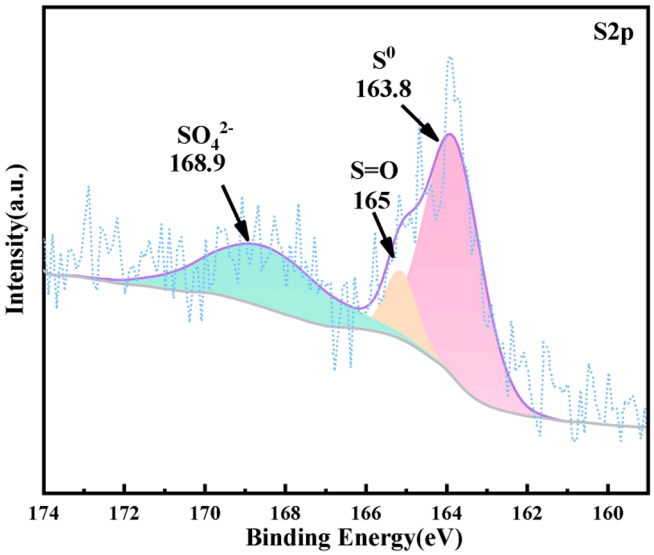

（b）HTH-800-10

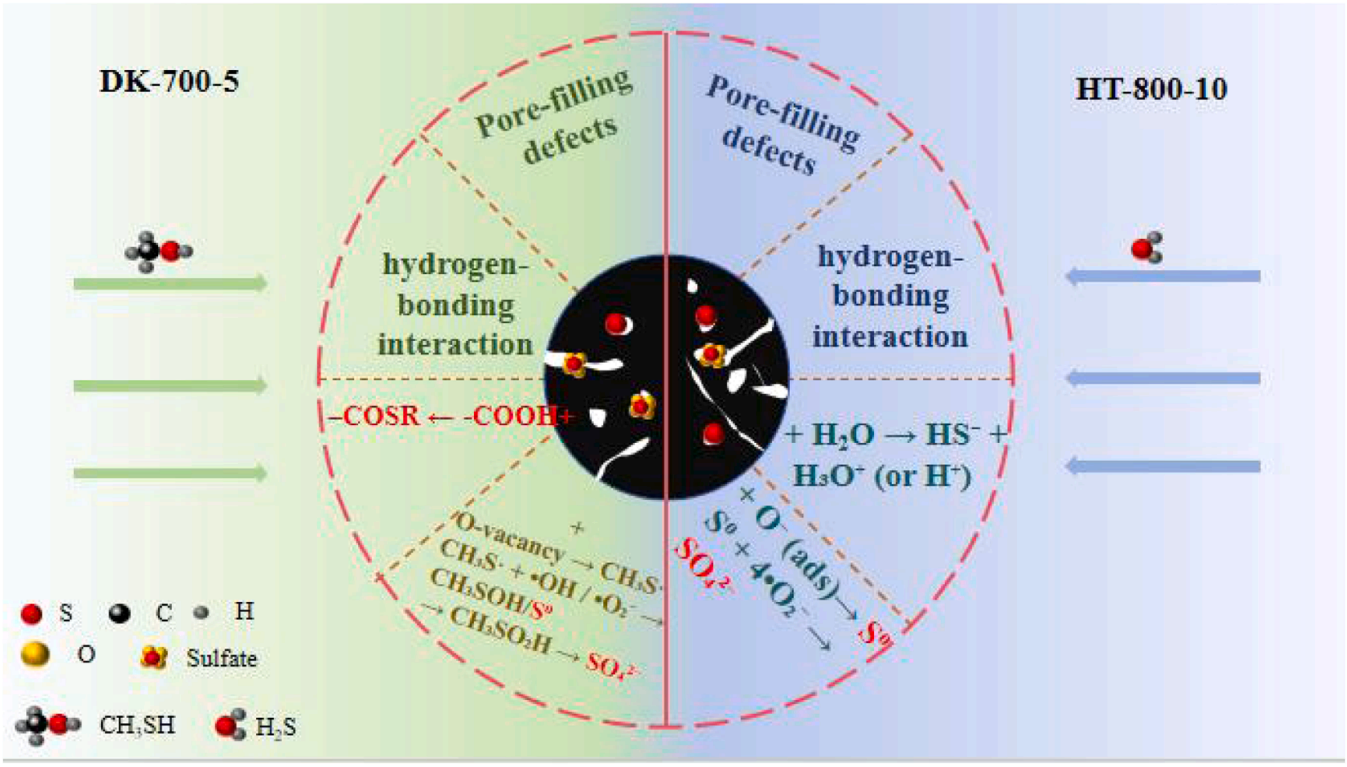

（c）Adsorption mechanism diagram

Fig. 16. S2p spectra and mechanism diagrams of DKH-700–5 and HTH-800–10.

the physisorption of CH_3SH molecules, while defect sites near oxygen vacancies enhance chemisorption. Oxygen vacancies can activate CH_3SH by weakening the S–H bond, generating nucleophilic CH_3S^-[35]. Adsorbed CH_3SH can be oxidized by superoxide radicals ($\cdot O_2^-$) formed from oxygen activated at these vacancies, producing intermediates such as methanesulfinyl (CH_3SOH) [36,37] and ultimately yielding sulfate ions (SO_4^{2-}), as evidenced by the high-binding-energy peak at 168.9 eV [38]. Incomplete oxidation results in residual elemental sulfur (S^0). Additionally, CH_3SH can interact with surface carboxyl groups via hydrogen bonding (–COOH···H–SCH_3) or react chemically to form thioesters (CH_3S–CO–) with concurrent H_2O release (CH_3SH + –COOH → CH_3S–CO– + H_2O) [25,26]. The CH_3S^- radical can react with hydroxyl radicals (•OH) to form the intermediate CH_3SOH, which may further undergo oxidation to higher sulfur-containing species (CH_3S^- + •OH → CH_3SOH) [39]. Overall, oxygen-containing functional groups and oxygen vacancies in DK-700–5 synergistically facilitate CH_3SH adsorption and oxidation, consistent with the enhanced oxygen and sulfur signals observed in DKH-700–5. The adsorption mechanism is detailed in Fig. 16 (c) and reaction Eqs. (2)-(7):

CH_3SH (gas) → CH_3SH(ads) (physisorption in pores & defects) (2)

CH_3SH(ads) + -C=O → H-bonding interaction (3)

$CH_3SH(ads) + \text{-}COOH \rightarrow$ possible thioester-like species (-S–CO-R) (4)

$CH_3SH(ads) + O\text{-vacancy} \rightarrow CH_3S^- + H^+$ (5)

$CH_3S^- + \bullet OH / \bullet O_2^- \rightarrow CH_3SOH / S^0$ (6)

$CH_3SOH \rightarrow CH_3SO_2H \rightarrow SO_4^{2-}$ (via stepwise oxidation) (7)

Fig. 16(b) presents the S 2p spectrum of HTH-800–10, showing that adsorbed sulfur exists predominantly as elemental sulfur (S^0) and oxidized sulfur species. The HT-800–10 surface adsorbs H_2S through a combination of physical adsorption and chemical interactions with active sites (C═O, C-O). The oxidation of H_2S by superoxide radicals ($\cdot O_2^-$) to form S^0 and sulfate ions (SO_4^{2-}) [23,40]. Elemental sulfur initially occupies the vacancies ($H_2S + O_2 \rightarrow S^0 + H_2O$), while continued oxidation by $\cdot O_2^-$ converts it into soluble sulfate, regenerating the active sites. The involvement of additional reactive oxygen species, such as ·OH, further accelerates H_2S oxidation. This mechanism highlights the critical roles of surface functional groups and vacancy-induced catalytic activity in enhancing H_2S adsorption and transformation on HT-800–10. The adsorption mechanism is illustrated in Fig. 16(c) and summarized in the following reactions (8)–(13):

$H_2S \rightarrow H_2S(ads)$ (physical adsorption of H_2S within pores and defects)(8)

$H_2S(ads) + \text{-}C{=}O/C\text{–}O \rightarrow H_2S(ads)\cdots$Surface groups (H-bonding interaction) (9)

$H_2S(ads) + H_2O \rightarrow HS^- + H_3O^+$ (or H^+) (10)

pyrrolic-N $+ H^+ \rightarrow$ pyrrolic-NH^+ (11)

$H_2S(ads) + O^-(ads) \rightarrow S^0 + H_2O$ (12)

$S^0 + 4\bullet O_2^- + 2H_2O \rightarrow SO_4^{2-} + 4OH^-$ (13)

Note: $H_2S(ads)$ denotes adsorbed hydrogen sulfide species.

3.3.3. Raman

After CH_3SH adsorption, the I_D/I_G ratio of DK-700–5 decreased from 1.016 to 0.925, indicating a reduction in defect density and an enhanced degree of graphitization. This trend can be attributed to both structural and chemical effects. The partial collapse or blockage of pore structures during adsorption reduces the proportion of disordered carbon regions. Simultaneously, surface reactions involving CH_3SH contribute to local carbon framework rearrangement: superoxide radicals ($\cdot O_2^-$) oxidize CH_3SH to sulfoxides, inducing structural reorganization of defect carbon; CH_3SH can also react with carboxyl groups to form thioesters or be activated at oxygen vacancies to generate CH_3S^- intermediates that integrate into the carbon matrix, filling structural defects. Collectively, these interactions decrease sp^3 -hybridized content while enhancing the ordering of sp^2 domains, as evidenced by the attenuation of the D-band and intensification of the G-band in the Raman spectra (Fig. 17).

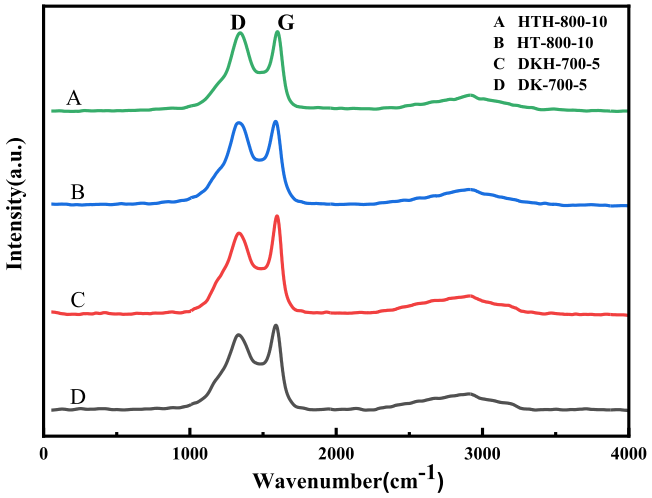

Fig. 17. Raman Spectrogram.

Similarly, after H_2S adsorption, the I_D/I_G ratio of HT-800–10 decreased from 1.081 to 1.017, reflecting partial defect passivation and local rearrangement of the carbon framework. The high specific surface area and well-developed pore structure of HT-800–10 facilitate the accumulation and adsorption of H_2S molecules. The subsequent deposition of sulfur-containing products (e.g., elemental sulfur or sulfates) partially blocks micropores, reducing disordered carbon regions [41]. Additionally, superoxide radicals ($\cdot O_2^-$) act as active sites promote stepwise H_2S oxidation [42], leading to local surface reconstruction and defect passivation. Compared with medium-temperature carbons, HT-800–10 exhibits higher structural stability, which accounts for the relatively moderate changes observed in its Raman spectra.

4. Conclusions

In this study, the adsorption capacities of silicon-modified biomass-derived graphitic carbons, DK-700–5 and HT-800–10, for sulfur-containing odorous gases (CH_3SH and H_2S) were systematically evaluated through physicochemical characterization and adsorption performance tests. Rice husk and pecan shell were mixed with sodium silicate and pyrolyzed, generating SiO_2 in situ. Subsequent high-concentration NaOH leaching removed most of the SiO_2 template while preserving the pore structures originally occupied by SiO_2, endowing DK-700–5 and HT-800–10 with enhanced adsorption performance. DK-700–5 exhibited an 8.3-fold increase in CH_3SH sulfur capacity compared to unmodified rice husk biochar, with a specific surface area of 297.05 m^2/g and an adsorption duration of 241 min. HT-800–10 showed a 2.45-fold improvement in H_2S adsorption relative to unmodified walnut shell biochar, achieving a specific surface area of 513.27 m^2/g and an adsorption time of 164 min.

The low-graphitized structures of both materials, characterized by abundant defects and edge sites, were identified as key contributors to their superior adsorption performance. DK-700–5 captured CH_3SH through both physical confinement and chemical interactions with surface functional groups (e.g., hydroxyl and carboxyl). Adsorbed CH_3SH was further oxidized by superoxide radicals ($\cdot O_2^-$) generated at oxygen vacancies, forming sulfate ions (SO_4^{2-}) with intermediate products including elemental sulfur (S^0) and sulfoxides (R-SO-R). HT-800–10 adsorbed and oxidized H_2S via surface active sites (e.g., C═O, C-O, $\cdot O_2^-$), producing sulfur-containing compounds such as sulfates, sulfides, and sulfur oxides, thereby achieving efficient adsorption and oxidative conversion.

These results indicate that optimized pyrolysis conditions promoted the formation of graphitic domains, while silicon-templating modification enhanced porosity and active site exposure. Both strategies effectively improved biochar adsorption capacities for CH_3SH and H_2S. This work provides valuable insights and data for the design of high-performance biomass-derived carbons for environmental odor control applications.

Author contribution

Ruiying Wang proposed the research topic, implemented the experimental process, and provided a final review of the paper. Fen Li sorted out the article data and organized papers. Ying Yang、Hong Yan and Oxana P.Taran reviewed the paper. Dongdong Yang revised the paper. All authors read and approved the final manuscript.

CRediT authorship contribution statement

Fen Li: Writing – review & editing, Funding acquisition,

Conceptualization. **Oxana P. Taran:** Supervision. **Hong Yan:** Supervision. **Ruiying Wang:** Writing – review & editing, Writing – original draft, Visualization, Methodology, Investigation, Formal analysis, Data curation, Conceptualization. **Dongdong Yang:** Supervision. **Ying Yang:** Supervision.

Funding

This work was supported by the National Natural Science Foundation of China Fund under Grant 22278100.

Declaration of Competing Interest

The authors declare that they have no known competing financial interests or personal relationships that could have appeared to influence the work reported in this paper.

Acknowledgments

The authors are very grateful to the editor and anonymous reviewers for their valuable comments and helpful suggestions.

Data availability

Data will be made available on request.

References

[1] Y. Long, S. Zhao, X. Tang, Q. Yu, F. Gao, J. Liu, H. Yi, Research status and prospect of purification technology of sulfur-containing odor gas, J. Environ. Sci. 149 (2025) 301–313.
[2] P.R. Robinson, Sulfur removal and recovery, Springe Handb. Pet. Technol. . (2017) 649–673.
[3] S.K. Kailasa, J.R. Koduru, K. Vikrant, Y.F. Tsang, R.K. Singhal, C.M. Hussain, K. H. Kim, Recent progress on solution and materials chemistry for the removal of hydrogen sulfide from various gas plants, J. Mol. Liq. 297 (2020) 111886.
[4] E. Glushchenko, A. Kadyseva, Wastewater deodorization: problems and solutions (December), in: In IOP Conference Series: Earth and Environmental Science, 937, IOP Publishing, 2021 042064 (December).
[5] Z. Zheng, X. Zhang, K. Li, H. Pi, B. Du, C. Li, X. Chen, Simultaneous treatment of various malodorous substances in gas by non-thermal plasma, IEEE Trans. Plasma Sci. 51 (2) (2023) 414–420.
[6] P.L. Kasper, A. Feilberg, Regenerative one-stage catalytic absorption process with cupric ions for removal of reduced sulfur compounds in polluted air, Environ. Technol. 44 (25) (2023) 3926–3936.
[7] Li, Q., Li, F., Yang, Y., Yan, H., & Yu, C. (2024). Adsorption mechanism of adsorbents for mercaptan foul-smelling substances: A review. Chemical Engineering Research and Design.
[8] A.T. Akintola, E.T. Akinlabi, S.O. Masebinu, Biochar as an adsorbent: a short overview. Valorization of biomass to Value-Added commodities, Curr. Trends Chall. Future Prospects (2020) 399–422.
[9] K.R. Gbangbo, A.R. Kouakou, A.D. Ehouman, B. Yao, G.V.E. Goli Lou, Z. Gnaboa, G. C. Bailly, Influence of water content on hydrogen sulfide adsorption in biogas purification with musa paradisiaca biochar, Chem. Afr. 6 (2) (2023) 657–665.
[10] Y. Chen, X. Zhang, W. Chen, H. Yang, H. Chen, The structure evolution of biochar from biomass pyrolysis and its correlation with gas pollutant adsorption performance, Bioresour. Technol. 246 (2017) 101–109.
[11] J. Qu, Y. Wang, X. Tian, Z. Jiang, F. Deng, Y. Tao, Y. Zhang, KOH-activated porous biochar with high specific surface area for adsorptive removal of chromium (VI) and naphthalene from water: affecting factors, mechanisms and reusability exploration, J. Hazard. Mater. 401 (2021) 123292.
[12] F. Wang, H. Sun, X. Ren, K. Zhang, Sorption of naphthalene and its hydroxyl substitutes onto biochars in single-solute and bi-solute systems with propranolol as the co-solute, Chem. Eng. J. 326 (2017) 281–291.
[13] P. Su, X. Gao, J. Zhang, R. Djellabi, B. Yang, Q. Wu, Z. Wen, Enhancing the adsorption function of biochar by mechanochemical graphitization for organic pollutant removal, Front. Environ. Sci. Eng. 15 (2021) 1–12.
[14] W. Gao, Z. Lin, H. Chen, S. Yan, H. Zhu, H. Zhang, Y. Wu, Roles of graphitization degree and surface functional groups of N-doped activated biochar for phenol adsorption, J. Anal. Appl. Pyrolysis 167 (2022) 105700.
[15] Y. Qin, B. Chai, C. Wang, J. Yan, G. Fan, G. Song, New insight into remarkable tetracycline removal by enhanced graphitization of hierarchical porous carbon aerogel: performance and mechanism, Colloids Surf. A Physicochem. Eng. Asp. 655 (2022) 130197.
[16] Q. Chen, Z. Wang, D. Long, X. Liu, L. Zhan, X. Liang, L. Ling, Role of pore structure of activated carbon fibers in the catalytic oxidation of H_2S, Ind. Eng. Chem. Res. 49 (7) (2010) 3152e3159, https://doi.org/10.1021/ ie901223j.
[17] A.C. Ferrari, J. Robertson, Interpretation of Raman spectra of disordered and amorphous carbon, Phys. Rev. B 61 (20) (2000) 14095.
[18] A.N. Mohan, B. Manoj, A.V. Ramya, Probing the nature of defects of graphene like nano-carbon from amorphous materials by Raman spectroscopy, Asian J. Chem. 28 (7) (2016) 1501.
[19] X. Luo, H. Zheng, W. Lai, P. Yuan, S. Li, D. Li, Y. Chen, Defect engineering of carbons for energy conversion and storage applications, Energy Environ. Mater. 6 (3) (2023) e12402.
[20] L.H. Zhang, Y. Shi, Y. Wang, N.R. Shiju, Nanocarbon catalysts: recent understanding regarding the active sites, Adv. Sci. 7 (5) (2020) 1902126.
[21] R.K. Sharma, J.B. Wooten, V.L. Baliga, X. Lin, W.G. Chan, M.R. Hajaligol, Characterization of chars from pyrolysis of lignin, Fuel 83 (11-12) (2004) 1469–1482.
[22] J. Zhao, W. Xiuwen, J. Hu, Q. Liu, D. Shen, R. Xiao, Thermal degradation of softwood lignin and hardwood lignin by TG-FTIR and Py-GC/MS, Polym. Degrad. Stab. 108 (2014) 133–138.
[23] Y. Li, Y. Lin, Z. Xu, B. Wang, T. Zhu, Oxidation mechanisms of H_2S by oxygen and oxygen-containing functional groups on activated carbon, Fuel Process. Technol. 189 (2019) 110–119.
[24] W. Qu, Z. Tang, H. Wen, M. Luo, T. Zhong, Q. Lian, D. Shu, Electron transfer trade-offs in MOF-derived cobalt-embedded nitrogen-doped carbon nanotubes boost catalytic ozonation for gaseous sulfur-containing VOC elimination, ACS Catal. 13 (1) (2022) 692–705.
[25] S. Detoni, D. Hadzi, Infra-red spectra of some organic sulphur-oxygen compounds, Spectrochim. Acta 11 (1956) 601–608.
[26] S. Pillai, J.W. Bozzelli, Computational study on structures, thermochemical properties, and bond energies of disulfide oxygen (S–S–O)-bridged CH_3SSOH and CH_3SS (= O) h and radicals, J. Phys. Org. Chem. 25 (6) (2012) 475–485.
[27] S.R. Kelemen, M. Afeworki, M.L. Gorbaty, P.J. Kwiatek, M.S. Solum, J.Z. Hu, R. J. Pugmire, XPS and ^{15}N NMR study of nitrogen forms in carbonaceous solids, Energy fuels 16 (6) (2002) 1507–1515.
[28] S. Bashkova, A. Bagreev, T.J. Bandosz, Adsorption of methyl mercaptan on activated carbons, Environ. Sci. Technol. 36 (12) (2002) 2777–2782.
[29] L.I. Feng, The effect of carbonyl, carboxyl and hydroxyl groups on the capacitance of carbon nanotubes, N. Carbon Mater. 26 (3) (2011) 224–228.
[30] M. Hu, Z. Ye, Q. Zhang, Q. Xue, Z. Li, J. Wang, Z. Pan, Towards understanding the chemical reactions between KOH and oxygen-containing groups during KOH-catalyzed pyrolysis of biomass, Energy 245 (2022) 123286.
[31] Z.R. Yue, W. Jiang, L. Wang, S.D. Gardner, C.U. Pittman Jr, Surface characterization of electrochemically oxidized carbon fibers, Carbon 37 (11) (1999) 1785–1796.
[32] J. Baltrusaitis, P.M. Jayaweera, V.H. Grassian, XPS study of nitrogen dioxide adsorption on metal oxide particle surfaces under different environmental conditions, Phys. Chem. Chem. Phys. 11 (37) (2009) 8295–8305.
[33] J. Deng, C. Gu, H. Xu, P. Zhu, G. Xiao, Oxygen vacancy-rich defects porous Cu2MgO3/Mg0. 78Cu0. 22O composite with sinter-resistant and highly reactive for long-duration high-temperature thermochemical energy storage, Adv. Funct. Mater. 34 (26) (2024) 2315529.
[34] Y. Ma, D. Kang, Y. Wen, Y. Chen, Y. Long, H. Yi, S. Zhao, Synergistic effects of pt single atomic site and cu nanoclusters for catalytic oxidation of methyl mercaptan, Appl. Surf. Sci. 657 (2024) 159718.
[35] Y. Jiang, Y. Fan, S. Li, Z. Tang, Photocatalytic methane conversion: insight into the mechanism of c (sp^3)–H bond activation, CCS Chem. 5 (1) (2023) 30–54.
[36] R.V. Kupwade, A concise review on synthesis of sulfoxides and sulfones with special reference to oxidation of sulfides, J. Chem. Rev. 1 (2) (2019) 99–113.
[37] Y. Li, X. Jiang, Green oxidation of sulfide to sulfoxide and sulfone, Green. Oxid. Org. Synth. (2019) 329–360.
[38] S. Bashkova, A. Bagreev, T.J. Bandosz, Adsorption of methyl mercaptan on activated carbons, Environ. Sci. Technol. 36 (12) (2002) 2777–2782.
[39] G. Zeng, M. Shi, M. Dai, Q. Zhou, H. Luo, L. Lin, X. Pan, Hydroxyl radicals in natural waters: light/dark mechanisms, changes and scavenging effects, Sci. Total Environ. 868 (2023) 161533.
[40] K.R. Olson, Y. Gao, F. Arif, K. Arora, S. Patel, E.R. DeLeon, K.D. Straub, Metabolism of hydrogen sulfide (H2S) and production of reactive sulfur species (RSS) by superoxide dismutase, Redox Biol. 15 (2018) 74–85.
[41] J. Li, Z. Su, C. Yu, Y. Yuan, Q. Wu, J. Liu, W. Huang, Recent progress in the development of sensing systems for in vivo detection of biological hydrogen sulfide, Dyes Pigments 192 (2021) 109451.
[42] F. Zhang, Z. Wei, G. Jiang, G. Li, M. Zhao, Z. Zhang, Z. Hao, Synergistic conversion of acid gases (H_2S and CO_2) to valuable chemicals: carbonyl sulfide synthesis over vacancy-defective CoMo sulfide catalysts, Appl. Catal. B Environ. 319 (2022) 121912.